

## REVIEW

[View Article Online](#)  
[View Journal](#) | [View Issue](#)Cite this: *Mater. Horiz.*, 2023,  
10, 1105Liquid-precursor-intermediated synthesis of  
atomically thin transition metal dichalcogenidesHuiyan Guan,<sup>†a</sup> Bei Zhao,<sup>†\*a</sup> Weiwei Zhao<sup>a</sup> and Zhenhua Ni<sup>id</sup> <sup>\*ab</sup>

With the rapid development of integrated electronics and optoelectronics, methods for the scalable industrial-scale growth of two-dimensional (2D) transition metal dichalcogenide (TMD) materials have become a hot research topic. However, the control of gas distribution of solid precursors in common chemical vapor deposition (CVD) is still a challenge, resulting in the growth of 2D TMDs strongly influenced by the location of the substrate from the precursor powder. In contrast, liquid-precursor-intermediated growth not only avoids the use of solid powders but also enables the uniform distribution of precursors on the substrate through spin-coating, which is much more favorable for the synthesis of wafer-scale TMDs. Moreover, the spin-coating process based on liquid precursors can control the thickness of the spin-coated films by regulating the solution concentration and spin-coating speed. Herein, this review focuses on the recent progress in the synthesis of 2D TMDs based on liquid-precursor-intermediated CVD (LPI-CVD) growth. Firstly, the different assisted treatments based on LPI-CVD strategies for monolayer 2D TMDs are introduced. Then, the progress in the regulation of the different physical properties of monolayer 2D TMDs by substitution of the transition metal and their corresponding heterostructures based on LPI-CVD growth are summarized. Finally, the challenges and perspectives of 2D TMDs based on the LPI-CVD method are discussed.

Received 28th September 2022,  
Accepted 9th December 2022

DOI: 10.1039/d2mh01207c

[rsc.li/materials-horizons](http://rsc.li/materials-horizons)

## 1. Introduction

Two-dimensional (2D) materials have increasingly shown great potential for (opto)electronic,<sup>1</sup> electrocatalytic,<sup>2</sup> and energy

storage<sup>3</sup> applications due to their unique dimensionality, layer-dependent adjustable band gap, diverse crystal structures, and other properties. With the rapid development of integrated electronic device technology,<sup>4–9</sup> the growth of large-area and high-quality 2D materials, especially TMD materials,<sup>5,10,11</sup> limits the transformation from theoretical research in the laboratory to large-scale industrial applications such as electronic devices.<sup>12–14</sup> Therefore, exploring controllable methods for the

<sup>a</sup> School of Physics, Southeast University, Nanjing 211189, China.

E-mail: zhni@seu.edu.cn

<sup>b</sup> Purple Mountain Laboratories, Nanjing 211111, China<sup>†</sup> These authors contributed equally to this work.

Huiyan Guan

Huiyan Guan received her BS Degree in Functional Materials from the Henan Normal University in 2022. Currently, she is an MA student at the School of Physics of Southeast University under the supervision of Prof. Zhenhua Ni and Prof. Bei Zhao. Her research is focused on the controllable synthesis of two-dimensional materials and their applications in electronics, and optoelectronics.



Bei Zhao

Dr Bei Zhao received her BS Degree in Materials Chemistry from Shandong University of Technology in 2014, her MA Degree in Applied Chemistry from Southwest University in 2017, and her PhD in Physical Chemistry from Hunan University in 2021. She has been an Associate Professor in Physics Department at Southeast University since December 2022. Her research is focused on the controllable synthesis of two-dimensional materials and their applications in electronics, and optoelectronics.



large-scale and industrial-scale synthesis of TMDs with uniform thickness becomes the key to facilitating scalable industrial applications for a range of electronic devices.<sup>15–17</sup> In this case, CVD<sup>18</sup> is one of the most promising method because of its low cost,<sup>19</sup> scalable material domain size,<sup>20</sup> and high controllability of thickness and uniformity,<sup>21</sup> attracting significant attention from researchers.<sup>22</sup> However, during the common CVD process,<sup>23</sup> it is difficult to control the vapor phase distribution and reaction rate of the solid precursor powder in the growth chamber.<sup>24</sup> The precursor concentration is not uniformly distributed on the substrate,<sup>19</sup> which will lead to the formation of local aggregation or local sparse non-uniform distribution of nucleation sites on the substrate,<sup>25</sup> resulting in the formation of undesirable nucleation and difficulty in controlling the nucleation density.<sup>26</sup> Although the introduction of a solid salt powder during the CVD process effectively reduces the high melting point of transition metal precursor powder, the distribution of the precursor concentration on the substrate in the growth chamber is still difficult to control.<sup>27</sup> Moreover, undesirable and inevitable byproducts or impurities will be introduced,<sup>28</sup> seriously decreasing the quality and influencing the stability of ultra-thin TMDs, leading to a poor electrical and optical performance.<sup>29</sup> Also, the byproducts and residual salts remain in the growth chambers and are difficult to remove,<sup>30</sup> thereby increasing the time and cost of cleaning or replacing the crucibles and quartz tubes.<sup>31</sup>

Recently, the LPI-CVD strategy has attracted great interest for the uniform wafer-scale growth of TMDs with high reproducibility, efficiency and scalability.<sup>27</sup> In the LPI-CVD process, the appropriate soluble precursor salt<sup>28</sup> such as Na<sub>2</sub>WO<sub>4</sub>, Na<sub>2</sub>MoO<sub>4</sub>, NaVO<sub>3</sub> and NaReO<sub>4</sub> is firstly dissolved in a certain solvent to achieve a uniform mixture of one or more precursors at the molecular level to form a precursor solution.<sup>32</sup> Subsequently,

the precursor solution is spin-coated on the substrate by adjusting the solution concentration and spin-coating speed to form an ultrathin film with the uniform distribution of each precursor source on the substrate.<sup>33</sup> Finally, as the growth temperature increases, the water in the spin-coated film gradually evaporates,<sup>34</sup> and the remaining solvent is uniformly distributed on the substrate in the molten state due to its lower melting point (650–850 °C),<sup>35</sup> making it easier to react with the gaseous sulfur precursors to produce uniform, high-quality and wafer-scale 2D TMD films such as MoS<sub>2</sub>,<sup>36</sup> MoSe<sub>2</sub>,<sup>37</sup> and WS<sub>2</sub>.<sup>38</sup> Moreover, the amount of each precursor source in the precursor solution can be precisely controlled by simply mixing molten salt aqueous solutions in designated ratios,<sup>39</sup> which is more conducive to achieve uniform doping to regulate the electrical and optical properties of TMDs.<sup>40</sup> Notably, the use of precursor solutions in the LPI-CVD method allows the formation of precursor films with specific patterns on the substrate,<sup>41</sup> which can then be templated to grow to form high-quality 2D TMDs arrays, which is difficult to achieve with powder precursors.<sup>42,43</sup> In addition, precursor films with a precisely controlled composition or thickness reduce the production of some undesirable byproducts and additional contaminants in the growth chamber during the growth process.<sup>44</sup> Herein, a systematic understanding based on existing typical works needs to be further established to set the stage for the future development of the LPI-CVD method.

Herein, we present a comprehensive review of the recent advances in the synthesis of 2D TMDs based on LPI-CVD growth, and the following contents include four parts. Firstly, various assisted treatments that enable the controlled synthesis of atomically thin 2D TMDs, such as direct synthesis, molten-salt assisted, hydroxide-assisted, polymer-assisted, and the supply of novel chalcogen precursors are presented in detail. Then, the developed techniques for regulating the different properties of atomically doped monolayer 2D TMDs are discussed, which are capable of achieving uniform large-area doping in a controlled way. Furthermore, we summarize the progress on the synthesis of heterostructures based on 2D TMDs using the LPI-CVD strategy with particular emphasis on its advantages. Finally, the challenges and perspectives in the future of liquid-precursor-intermediated synthesis of 2D TMDs are prospected, showing the potential opportunities in realizing a technological revolution by LPI-CVD in TMD systems.

## 2 Synthesis of monolayer 2D TMDs materials

The LPI-CVD method allows the film thickness to be controlled by adjusting the solution concentration and spin-coating speed, which is a huge advantage for the growth of large-area 2D TMDs growth.<sup>27</sup> The successful implementation of LPI-CVD requires the following conditions: (I) the precursor salts must have a suitable melting point and dissolve in suitable solvents (such as H<sub>2</sub>O). (II) Precursor salts that tend to form stable low vapor pressure melts at LPI-CVD growth temperatures. (III) The substrate must be hydrophilic, which can be treated by oxygen



**Zhenhua Ni**

*Dr Zhenhua Ni received his BS Degree in Physics and a second BS Degree in Applied Electrical Techniques from Shanghai Jiao-tong University in 2003 and PhD in Physics from the National University of Singapore (NUS) in 2007. Subsequently, he did postdoctoral research in the Department of Physics and Applied Physics at Nanyang Technological University (NTU) from 2007–2010. In 2009, he received the British Council “Researcher*

*Exchange Programme Award” and worked as an academic visitor in Andre Geim’s research group in the University of Manchester. He has been a Professor in Physics Department at Southeast University since May 2010. His current research interests include the fabrication, characterization, and optoelectronic application of graphene and other two-dimensional materials.*



plasma, UV-O<sub>3</sub>, and piranha solution. Furthermore, various assisted techniques have been implemented to promote the lateral growth of 2D TMDs such as molten-salt assisted, hydroxide-assisted, polymer-assisted, and supply of novel chalcogen precursors, which will be summarized in this section.

## 2.1 Direct LPI-CVD growth

In the common CVD, a powder precursor such as MoO<sub>3</sub>, WO<sub>3</sub>, sulfur powder and selenium powder is used to obtain 2D TMDs.<sup>45–47</sup> However, the gas atmosphere generated by the evaporation of the precursor powder in the growth chamber is difficult to control,<sup>23</sup> causing the precursor concentration to be non-uniformly distributed on the substrate and the nucleation density uneven.<sup>48</sup> The use of liquid precursors solves the problem of non-uniform distribution of the precursor concentration on the substrate and opens a new path for the growth of ultrathin 2D TMDs.<sup>49</sup> In 2012, Liu *et al.* firstly demonstrated the production of large-area MoS<sub>2</sub> films on insulating substrates by using (NH<sub>4</sub>)<sub>2</sub>MoS<sub>4</sub> solution as the Mo source precursor.<sup>50</sup> However, the synthesis of uniform monolayer MoS<sub>2</sub> films was not achieved, and this dip-coating method only achieved the growth of triple MoS<sub>2</sub> films with two layers appearing locally, as shown in Fig. 1(b). This can be attributed to the fact that the dip-coating process does not ensure a uniform distribution of the precursor solution on the substrate surface, and too many Mo sources on the substrate make it difficult to form a thinner MoS<sub>2</sub> film (Fig. 1(a)).

In contrast, the spin-coating process has a huge advantage in ensuring that the precursor solution forms a uniform film thickness at all locations on the substrate surface by precisely

controlling the spin rate, spin time and other parameters. Cun *et al.* successfully achieved the growth of wafer-scale monolayer MoS<sub>2</sub> films by the spin-coating process with the uniform distribution of Mo nucleation sites (Fig. 1(c)–(e)).<sup>36</sup> Similarly, NaMoO<sub>4</sub> particles uniformly distributed on the substrate by spin coating will melt into liquid, while high-quality MoS<sub>2</sub> films with high electrical performance (Fig. 1(f)–(i)) will be synthesized when the sulfur vapor is saturated with liquid droplets.<sup>51,52</sup> Furthermore, other 2D materials such as 2-inch continuous WS<sub>2</sub> films<sup>38</sup> and continuous Bi<sub>2</sub>O<sub>2</sub>Se films<sup>53</sup> with the thickness of few atomic layers have also been successfully obtained *via* the LPI-CVD method. Furthermore, industrial inkjet-printer was used in the LPI-CVD system to prepare monolayer TMDs such as MoSe<sub>2</sub> and MoS<sub>2</sub> with millimeter size, in which an aqueous solution of (NH<sub>4</sub>)<sub>6</sub>Mo<sub>7</sub>O<sub>24</sub>·4H<sub>2</sub>O was used as the precursor solution.<sup>54</sup> Therefore, the LPI-CVD method is still feasible for the large-area ultrafast and patterned growth of high-quality TMDs under suitable conditions, with good prospects for industrialization, which requires more research in the future.

## 2.2 Molten-salt-assisted LPI-CVD growth

In general, by using alkali metal halide mixed directly with solid source powders as precursors, TMD films will inevitably grow in the vapor–solid–solid (VSS) growth mode, sometimes accompanied by the vapor–liquid–solid (VLS) growth mode. In comparison, a promising feature of the molten salt-assisted approach is that the molten salt and the transition metal source can be homogeneously mixed in the liquid state at the molecular level, which ensures their uniform distribution on the substrate

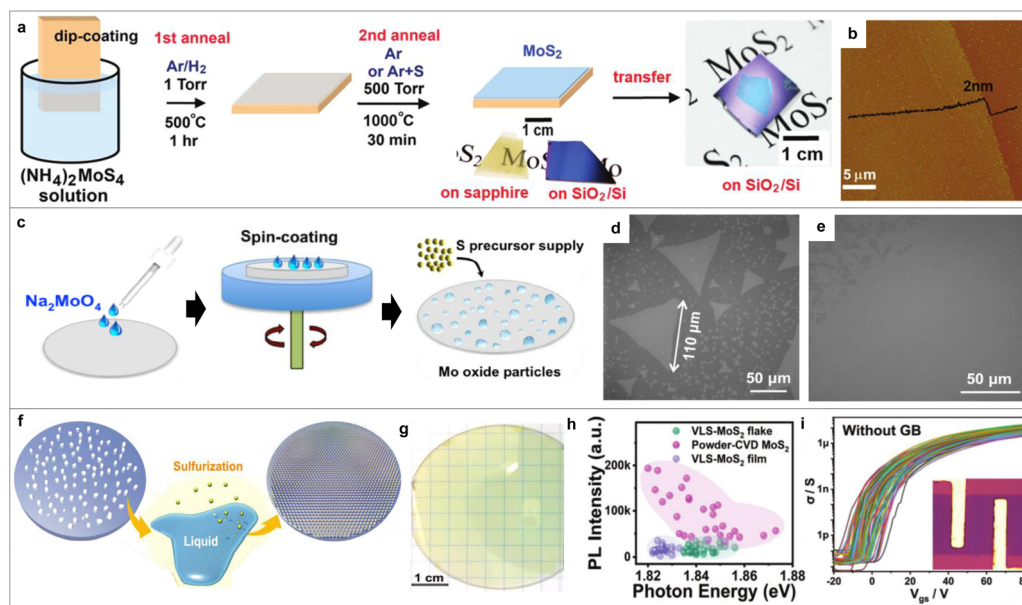


**Fig. 1** (a) Illustration of the synthesis of MoS<sub>2</sub> layers. Inset is the optical image of MoS<sub>2</sub> film.<sup>50</sup> (b) AFM image of the triple MoS<sub>2</sub>.<sup>50</sup> (c) Illustration of the synthesis of monolayer MoS<sub>2</sub>.<sup>36</sup> (d) Optical image of MoS<sub>2</sub> flake.<sup>36</sup> (e) Optical image of continuous MoS<sub>2</sub> film.<sup>36</sup> (f) Illustration of the V-S-L growth mechanism for MoS<sub>2</sub> films.<sup>52</sup> (g) Optical image of monolayer MoS<sub>2</sub> film on a sapphire substrate.<sup>52</sup> (h) PL distribution of three types of MoS<sub>2</sub> samples.<sup>52</sup> (i) Transport curves of FETs based on MoS<sub>2</sub> without the growth of GB.<sup>49</sup> (a) and (b) Reprinted from ref. 50 Copyright 2012, the American Chemical Society. (c)–(e) Reprinted from ref. 36 Copyright 2019, Springer Nature. (f)–(i) Reprinted from ref. 52 Copyright 2019, The Royal Society of Chemistry.



surface by spin-coating, ink-jet printing, and other processes, efficient interaction with the transition metal source and stable synthesis of TMDs in a single VLS growth mode. For example, Ji *et al.* successfully synthesized millimeter-size monolayer MoS<sub>2</sub> films by using (NH<sub>4</sub>)<sub>2</sub>MoO<sub>4</sub> and KI as precursors *via* the LPI-CVD method (Fig. 2(a)).<sup>55</sup> The presence of KI in the growth lower the MoS<sub>2</sub> reaction barrier. According to the edge passivation-substitution (EPS) theoretical growth model shown in Fig. 2(b), this reduction in the reaction potential barrier is attributed to the passivation of the Mo atom zigzag edges by halogen atoms. The Mo–X bond will be replaced by an Mo–S bond during the sulfuration reaction, decreasing the reaction potential barrier compared to the oxygen atom passivation-substitution process, which greatly facilitates the growth of millimeter-size MoS<sub>2</sub> monolayer (Fig. 2(c)). For common alkali metal halides such as NaCl and KI, their alkali metals can liquefy and stabilize transition metal oxides (TMOs), their halogen elements are capable of reacting with TMOs to form metal oxychlorides with low melting points, and the synergistic effect of the two can significantly reduce the formation energy of the material. The addition of KI produced uniform and continuous high-quality MoSe<sub>2</sub> films (Fig. 2(d)) in which KI significantly reduced the energy barrier of chalcogenization and promoted the lateral growth of MoSe<sub>2</sub> along the in-plane.<sup>34</sup> Besides MoS<sub>2</sub> and MoSe<sub>2</sub>, the KI-assisted LPI-CVD method can also be used for the growth of WS<sub>2</sub> (Fig. 2(e) and WSe<sub>2</sub> (Fig. 2(f)).<sup>56</sup>

In addition, besides the common alkali metal halide, some molten salts with the chemical formula A<sub>x</sub>MO<sub>y</sub> (where A is an alkali metal and M is a transition metal or sulfur group element) not only can serve as precursors for the growth of 2D TMDs by themselves, such as Na<sub>2</sub>SeO<sub>3</sub> and Na<sub>2</sub>TeO<sub>3</sub>, but can also effectively reduce the formation energies of TMDs (Fig. 2(g) and (h)), making it a new salt-assisted LPI-CVD method. For example, Li *et al.* synthesized continuous-monolayer MoSe<sub>2</sub> films with a grain size of 100–250 μm by mixing Na<sub>2</sub>MoO<sub>4</sub>–Na<sub>2</sub>SeO<sub>3</sub>.<sup>57</sup> Compared with only Na<sub>2</sub>MoO<sub>4</sub> molten salt, the mixed molten salt formed by adding Na<sub>2</sub>SeO<sub>3</sub> molten salt not only made the produced film more homogeneous but also significantly lowered the reaction potential and promoted the domain size of the monolayer MoSe<sub>2</sub>. With an increase in temperature, Na<sup>+</sup> can stabilize MoO<sub>4</sub><sup>2–</sup> and promote the growth of MoSe<sub>2</sub> in concert with SeO<sub>3</sub><sup>2–</sup>. Similarly, ReSe<sub>2</sub> and WTe<sub>2</sub> with improved yield have also been synthesized by using NaReO<sub>4</sub>–Na<sub>2</sub>SeO<sub>3</sub> and Na<sub>2</sub>WO<sub>4</sub>–Na<sub>2</sub>TeO<sub>3</sub> as precursors, respectively.

As research progresses, the molten-salt-assisted growth mechanism is increasingly being understood and the growth behavior is also becoming more controllable. Recently, Jiang *et al.* reported a new self-expanding molten salt-driven growth mechanism and successfully achieved the patterned growth of highly crystalline TMD arrays.<sup>58</sup> At a lower temperature, the Na<sub>2</sub>Se<sub>x</sub> (formed by Se with NaCl) reacts with Na–W–O intermediates (produced by WO<sub>3</sub> and NaCl) to form WSe<sub>2</sub> nuclei at

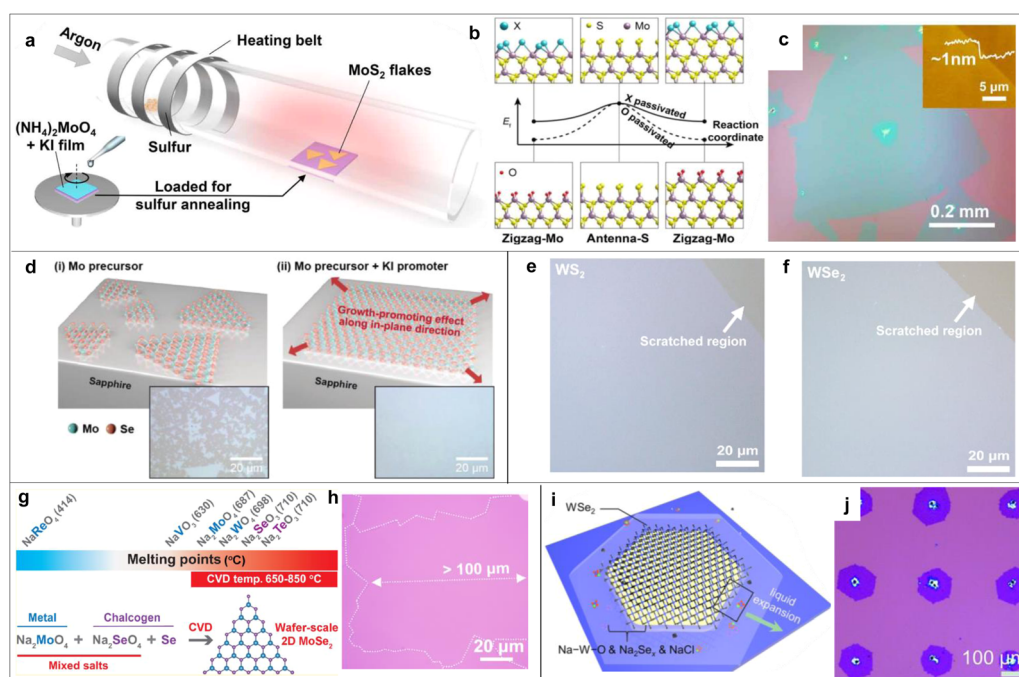


**Fig. 2** (a) Schematic of the synthesis of MoS<sub>2</sub> flakes.<sup>55</sup> (b) Energy barrier diagram for MoS<sub>2</sub> growth with (top) and without (bottom) KI and the edge structure.<sup>55</sup> (c) Optical image of MoS<sub>2</sub> flakes, inset is the AFM height image of MoS<sub>2</sub> edge.<sup>55</sup> (d) Illustration of MoS<sub>2</sub> growth with and without KI, inset is the optical image of MoS<sub>2</sub> film.<sup>34</sup> Optical image of continuous WS<sub>2</sub> (e) and WSe<sub>2</sub> film (f).<sup>56</sup> (g) Illustration of the melting points of some precursors, and schematic of the synthesis of MoSe<sub>2</sub> film.<sup>57</sup> (h) Optical image of monolayer MoSe<sub>2</sub> film with grain boundaries.<sup>57</sup> (i) Illustration of the self-expanding molten salt-driven mechanism for growing WSe<sub>2</sub> films.<sup>58</sup> (j) Optical image of WSe<sub>2</sub> array.<sup>58</sup> (a)–(c) Reprinted from ref. 55 Copyright 2021, American Association for the Advancement of Science. (d) Reprinted from ref. 34 Copyright 2022, Wiley-VCH. (e) and (f) Reprinted from ref. 56 Copyright 2021, the American Chemical Society. (g) and (h) Reprinted from ref. 57 Copyright 2021, the American Chemical Society. (i) and (j) Reprinted from ref. 58 Copyright 2022, the American Chemical Society.



designed sites, which then continuously extend horizontally and vertically. The molten salt in the interlayer between the TMD edge and the substrate confines the reaction sites (Fig. 2(i)). Due to the non-wetting effect of the TMDs, the molten salt keeps spreading to the edge and provides a reaction source, and the monolayer TMDs keep expanding until the molten salt is depleted. The obtained TMD arrays (Fig. 2(j)) present new ideas for the preparation of wafer-scale and single-crystal TMDs. The deeper exploration of the molten-salt assisted method and its development and application deserve more efforts for further research.

### 2.3 Hydroxide-assisted LPI-CVD growth

The novel design of precursor solutions can open up new ideas for the growth of 2D TMD films. Unlike other promoters that produce unavoidable residues, the introduction of hydroxyl groups not only can be effectively removed by temperature regulation, but also shows amazing advantages in promoting the monolayer growth of TMDs. In 2019, Zhu *et al.* reported an MoS<sub>2</sub>-OH bilayer-mediated method to successfully grow one-inch uniform monolayer MoS<sub>2</sub> films.<sup>59</sup> The added KOH forms homogeneous mixture of solutions, which can generate -OH, the key to hydroxide-assisted growth. When the -OH group is not present in the precursor solution (Fig. 3(a)), the Mo atoms directly combine with sulfur atoms on the substrate to form multilayer MoS<sub>2</sub>. When the -OH group is introduced in the

precursor solution, as shown in Fig. 3(b), the Mo atoms and sulfur atoms are combined in the substrate to firstly form monolayer MoS<sub>2</sub>, and then the -OH group will be adsorbed on the monolayer MoS<sub>2</sub> (100) surface to form an MoS<sub>2</sub>-OH bilayer structure. The presence of the -OH group layer on the MoS<sub>2</sub> (100) surface makes the Mo atoms and sulfur atoms adsorbed only on the edge of the first MoS<sub>2</sub> layer, preventing the growth of MoS<sub>2</sub> along the [001] axis to form multilayers and promoting its growth in the lateral direction, leading to the preferential formation of ultra-large monolayer MoS<sub>2</sub>. Fig. 3(c) clearly demonstrates the uniformity of the monolayer MoS<sub>2</sub> films with full coverage on 1 × 1 and 3 × 3 cm<sup>2</sup> sapphire obtained by the hydroxide-assisted LPI-CVD method. In addition, the binding energy of MoS<sub>2</sub> is -0.24 eV with the introduction of -OH groups, which is lower than the corresponding binding energy without -OH groups (Fig. 3(d)), confirming that the introduction of -OH groups reduces the energy barrier for the growth of monolayer MoS<sub>2</sub>.

Similar to the effect produced in promoting the growth of MoS<sub>2</sub> monolayers, the introduction of hydroxyl groups can also have an effect on the modulation of TMD shape. The presence of the OH<sup>-</sup> could modulate the morphology of NbSe<sub>2</sub>, which could anchor the Nb precursor.<sup>60</sup> With an increase in the -OH and Nb concentration, the edge growth rate of the Se terminal was faster than that of the Nb terminal, and thus the shape of NbSe<sub>2</sub> changed from hexagonal to triangular, tripod-like, and

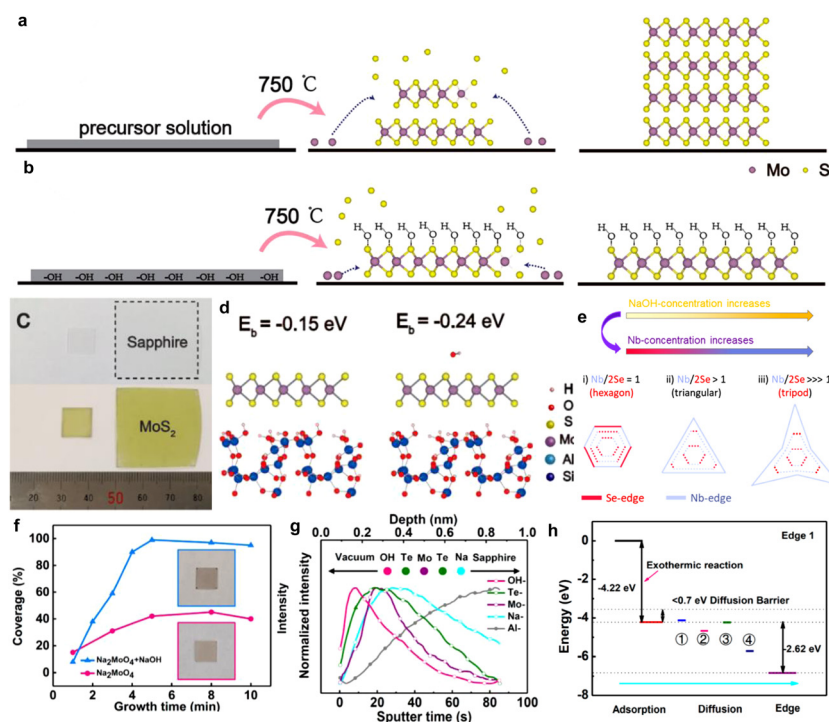


**Fig. 3** Illustration of MoS<sub>2</sub> growth with (a) and without NaOH (b).<sup>59</sup> (c) Optical micrograph of MoS<sub>2</sub> on sapphire substrate.<sup>59</sup> (d) Atomic structure of MoS<sub>2</sub> with and without NaOH and the corresponding calculated binding energies.<sup>59</sup> (e) Transformation diagram of NbSe<sub>2</sub> morphology at different NaOH or Nb concentrations.<sup>60</sup> (f) MoTe<sub>2</sub> coverage at different precursor solutions and inset is the optical image of MoTe<sub>2</sub> films.<sup>61</sup> (g) Time-of-flight secondary ion mass spectrometry (ToF-SIMS) of MoTe<sub>2</sub> growth with NaOH.<sup>61</sup> (h) Calculated reaction energy diagram of MoTe<sub>2</sub> molecule adsorbed on the surface of MoTe<sub>2</sub> monolayer.<sup>61</sup> (a)–(d) Reprinted from ref. 59 Copyright 2019, the American Chemical Society. (e) Reprinted from ref. 60 Copyright 2020, the American Chemical Society. (f)–(h) Reprinted from ref. 61 Copyright 2021, the American Chemical Society.



herringbone-like (Fig. 3(e)). In addition, a centimeter-sized monoclinic  $\text{MoTe}_2$  monolayer with almost 100% coverage (Fig. 3(f)) has also been successfully achieved using the hydroxide-assisted LPI-CVD method.<sup>61</sup> The time-of-flight secondary ion mass spectrometry (ToF-SIMS) images showed that the  $-\text{OH}$  introduced from the precursor solution could adsorb on the surface (Fig. 3(g)) of the material to form an  $-\text{OH}$  layer, which inhibited the growth of the material in the vertical direction. DFT calculations showed that the diffusion potential of less than 0.7 eV for different diffusion paths of  $\text{MoTe}_2$  molecules from the surface to the edge and the adsorption energy at the edges is smaller than that at the surface (Fig. 3(h)), which indicates that  $\text{MoTe}_2$  molecules can diffuse on the surface and adsorb more preferentially at the edge sites, leading to the lateral growth of  $\text{MoTe}_2$ . This success, which has the same effect as the promotion of monolayer  $\text{MoS}_2$  growth described above, indicates that the hydroxide-assisted LPI-CVD growth method has the potential to be extended to the monolayer of other TMDs growth and can provide a simple and universal idea for the growth of ultrathin TMDs.

## 2.4 Polymer-assisted LPI-CVD growth

Besides water, organic solutions have been also used as the basic solvent, such as dimethylformamide (DMF), *n*-butylamine, ethylenediaminetetraacetic acid (EDTA), and dimethyl sulfoxide

(DMSO), for the growth of TMDs. By adding complexing agents, hydrogen and coordination bonds are formed with the soluble salt in solution, which in turn form stable polymers to improve the controllability and homogeneity of the precursor films during spin coating. In 2015, Yang *et al.* successfully synthesized 2-inch wafer-scale homogeneous  $\text{MoS}_2$  films with excellent thickness controllability (Fig. 4(a)) by optimizing the solvent for dissolving  $(\text{NH}_4)_2\text{MoS}_4$ .<sup>62</sup> When the solvent contained only DMF (Fig. 4(b)), the  $\text{MoS}_4^{2-}$  group could not be completely dissolved, leaving a precursor film with de-wetted areas and pinholes. When 2-aminoethanol was added in DMF solvent (Fig. 4(c)), its functional group hydroxide group could join with the  $\text{MoS}_4^{2-}$  group to form hydrogen bonds, which allowed the  $\text{MoS}_4^{2-}$  group to be uniformly distributed in the solution, and eventually form a uniform precursor film, while it still had certain micro-scale defects. When *n*-butylamine was added to the achieved solvent (Fig. 4(d)), an almost defect-free  $\text{MoS}_4^{2-}$  group film was achieved. In addition, as shown in Fig. 4(e) and (f), the linear-poly(ethylenimine) (L-PEI) in the precursor solution is ionically bonded to the anhydrous ammonium tetrathiomolybdate (ATM) to form a complex precursor, which facilitates uniform spin coating of large areas and reduces the de-wetting areas,<sup>63</sup> and therefore 6-in wafer-scale  $\text{MoS}_2$  films were more readily available. Noteworthy, L-PEI can be decomposed directly without carbon residue at relatively low temperature, which avoids contamination

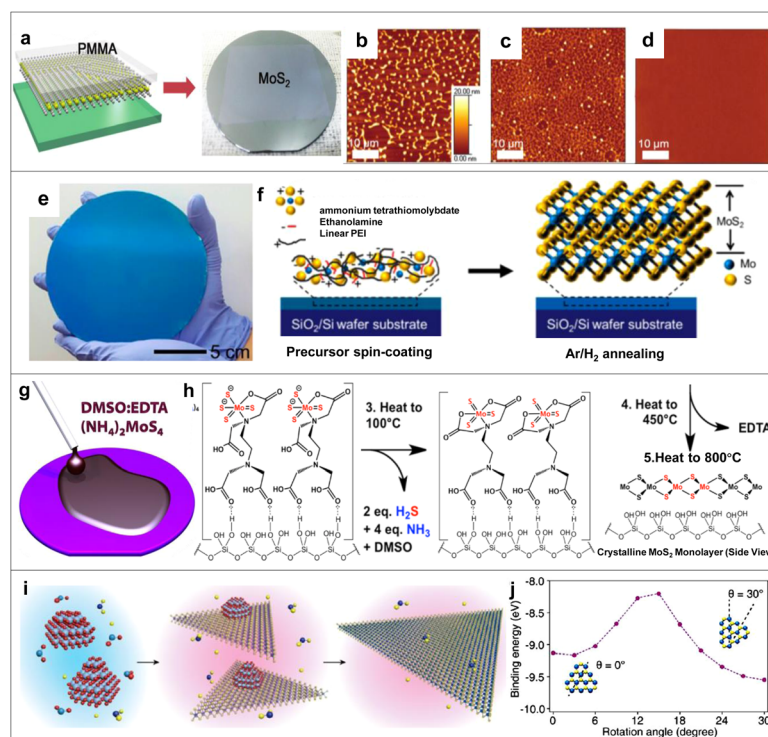


**Fig. 4** (a) Transfer process of  $\text{MoS}_2$  film.<sup>62</sup> (b)–(d) AFM images of different precursor films: (b) only DMF, (c) DMF : 2-aminoethanol (9 : 1), and (d) DMF : *n*-butylamine : 2-aminoethanol in a volume ratio of 4.5 : 4.5 : 1.<sup>62</sup> (e) Optical image of  $\text{MoS}_2$  film.<sup>63</sup> (f) Schematic of the synthesis of  $\text{MoS}_2$  films.<sup>64</sup> (g) Schematic of the synthesis of  $\text{MoS}_2$  film.<sup>64</sup> (h) Growth mechanism of  $\text{MoS}_2$  films.<sup>64</sup> (i) Growth mechanism of  $\text{MoS}_2$  films.<sup>65</sup> (j) Binding energy curves of  $\text{MoS}_2$  and  $\text{MoO}_3$  at different rotation angles.<sup>65</sup> (a)–(d) Reprinted from ref. 62 Copyright 2015, The Royal Society of Chemistry. (e) and (f) Reprinted from ref. 63 Copyright 2017, The American Chemical Society. (g) and (h) Reprinted from ref. 64 Copyright 2017, Springer Nature. (i) and (j) Reprinted from ref. 65 Copyright 2021, the American Chemical Society.



during the growth process. Compared to the use of DMF and L-PEI, the introduction of other organic solvents such as chelating agents not only can reduce the dehumidification of precursor films on the substrate surface, but also interact with the precursor source in solution to increase the coverage of the precursor on the substrate surface, which is also conducive to achieve the growth of wafer-scale MoS<sub>2</sub> films.<sup>64</sup> In the precursor solution, EDTA coordinates with the MoS<sub>4</sub><sup>2−</sup> anion in DMSO to form hydrogen bonds and produce a complex precursor solution (Fig. 4(g)). When spin-coating the precursor solution, each carboxyl group from EDTA interacts with the hydroxyl group of the substrate, which anchors the precursor to the surface. Upon heating, DMSO first evaporates and releases H<sub>2</sub>S and NH<sub>3</sub> gases, leaving equal amounts of MoS<sub>3</sub> to form ligand bonds with equal amounts of EDTA (Fig. 4(h)). Then, EDTA evaporates at high temperature, causing MoS<sub>3</sub> to be uniformly distributed on the surface with hydroxyl terminations, and finally MoS<sub>3</sub> is reduced to crystalline MoS<sub>2</sub> films. This provides a new approach to synthesize large-area monolayer TMDs; however, the selection of the polymers used still needs further updating to better achieve the targeted and uniform distribution of precursors on the substrate surface. Recently, Kim *et al.* used colloidal nanoparticles with the uniform distribution of precursors on a nanometer scale as precursors to achieve the generation of wafer-scale MoS<sub>2</sub> films.<sup>65</sup> The MoO<sub>2</sub> nanoparticle precursors were formed *via* the polyvinyl-pyrrolidone (PVP)-assisted hydrothermal method, which were uniformly distributed on the substrate by the spin-coating process. At the beginning of sulfur supply growth, polycrystalline MoO<sub>2</sub> nanoparticles start to unfold laterally (Fig. 4(i)) and continuously transform into nanocrystals with single domains. Then, monolayers of MoS<sub>2</sub> nucleate at the bottom of MoO<sub>2</sub> nanoparticles with the lowest energy orientation angle (Fig. 4(j)). Finally, until the MoO<sub>2</sub> particles are depleted, the wafer-scale MoS<sub>2</sub> monolayer is synthesized on the substrate. It is worth noting that some appropriate organic solvents can evaporate without leaving residues during the ramp-up process, effectively avoiding the generation of contaminants. However, there are still many organic solvents with unavoidable residual problems, and therefore the selection of better organic solvents that effectively reduce the dehumidification of the precursor films and can more precisely control the coverage of the precursors on the substrate surface is worth further exploration and research.

### 2.5 Novel chalcogen precursor-supplied LPI-CVD growth

The transition metal precursor powder can be replaced by the corresponding soluble salt in the LPI-CVD method, allowing the transition metal precursor sources to be uniformly distributed on the substrate. However, the gas distribution of the chalcogen source in the chamber is still difficult to control. Therefore, it is equally critical to design a uniform and appropriate amount of chalcogen to control the flow on the substrate surface. In 2017, Boandoh *et al.* proposed a novel method to synthesize large-area MoS<sub>2</sub> films by precisely controlling the bubbling systems of the supply of chalcogen organics in the LPI-CVD method.<sup>66</sup> When Ar is passed through a bubbler into liquid dimethyl disulfide (DMDS), the DMDS enters the growth

chamber in the form of bubbles, which contains Mo(CO)<sub>6</sub> to supply the Mo source (Fig. 5(a)) and promote the growth of the Mo terminal edges. DMDS continuously decomposes into methyl mercaptan (CH<sub>3</sub>SH), ethylene (CH<sub>2</sub>CH<sub>2</sub>), and hydrogen sulfide (H<sub>2</sub>S) and other sulfides during the growth process, while Mo(CO)<sub>6</sub> decomposes into Mo radicals and undergoes the sulfidation reaction (Fig. 5(b)). The amount of sulfur precursors can be precisely controlled by controlling the flow rate of DMDS, resulting in the formation of large-area MoS<sub>2</sub> monolayer films (Fig. 5(c)). Similarly, dodecyl mercaptan (C<sub>12</sub>H<sub>25</sub>SH) could also be used as the sulfur source to synthesize uniform MoS<sub>2</sub> monolayers through LPI-CVD with a bubbling system.<sup>67</sup> Thiol (C<sub>12</sub>H<sub>25</sub>SH) as the sulfur source could precisely control the precursor concentration during the growth process (Fig. 5(d)), and also effectively repair the sulfur vacancies in the MoS<sub>2</sub> material (Fig. 5(d)–(f)). This novel sulfur supply method opens new horizons for the introduction of sulfur in common CVD systems with certain scalability as well as reproducibility. It effectively avoids the difficulty in controlling the gas-phase distribution generated by conventional solid sulfur sources.

In addition to the use of a bubbler, the use of temperature to control the decomposition of raw materials for the sulfur supply, such as Na<sub>2</sub>SO<sub>4</sub> could regulate the supply of sulfur to successfully synthesize WS<sub>2</sub>, MoS<sub>2</sub> and ZrS<sub>2</sub>.<sup>68</sup> At controlled temperatures above 700 °C, the Na<sub>2</sub>S generated by the decomposition of Na<sub>2</sub>SO<sub>4</sub> under a reducing atmosphere reacted with WO<sub>3</sub> on the substrate to form liquid Na<sub>2</sub>WO<sub>4</sub> and gaseous H<sub>2</sub>S as a transition metal source and sulfur source (Fig. 5(g)). The gaseous H<sub>2</sub>S is incorporated into the liquid Na<sub>2</sub>WO<sub>4</sub>, causing it to be released slowly to ensure a stable supply of sulfur source, and eventually some of the vaporized Na<sub>2</sub>WO<sub>4</sub> and H<sub>2</sub>S are transferred to the surface of the substrate to react with each other, synthesizing monolayer WS<sub>2</sub> (Fig. 5(h)). Furthermore, high-quality monolayer TMDs can also be obtained by designing new LPI-CVD growth methods to control the gas distribution of the solid chalcogen precursors. By placing the substrate in a one-end-closed inner quartz tube, the sulfur precursor pressure in the growth chamber changes from the gradient distribution presented in the common CVD process to a quasi-static distribution, whose distribution concentration of sulfur precursors on the surface of the substrate changes from high to low. The sulfur atoms will migrate to the energy favorable sites with low potential energy under the guidance of the substrate structure, resulting in the highly oriented growth of TMD domains with excellent electrical properties.<sup>69</sup> By precise controlling the precursor mass flux, these ingenious designs provide extremely important references for the future exploration of novel methods for the controlled growth of 2D TMDs.

## 3. Transition-metal substitution of 2D TMD materials

In the common CVD, it is often difficult to precisely control the mixture of vaporized host precursor with dopant, making the synthesis of high-quality and uniformly doped 2D TMDs a great



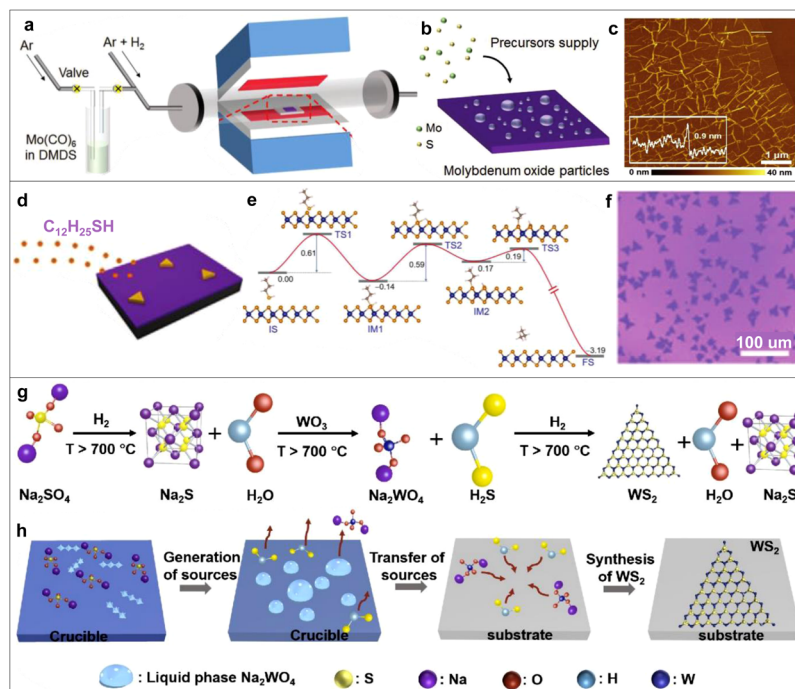


Fig. 5 (a) Illustration of the bubbling system.<sup>66</sup> (b) Schematic of the synthesis of MoS<sub>2</sub> film.<sup>66</sup> (c) AFM image of the MoS<sub>2</sub> film, where the white line shows the height of the film.<sup>66</sup> (d) Diagram showing the process of supplying thiol molecules.<sup>67</sup> (e) Potential diagram of thiol molecule repairing sulfur vacancy process.<sup>67</sup> (f) Optical images of MoS<sub>2</sub> films.<sup>67</sup> (g) Illustration of three-step chemical reaction process.<sup>68</sup> (h) Illustration of WS<sub>2</sub> growth process.<sup>68</sup> (a)–(c) Reprinted from ref. 66 Copyright 2017, Wiley-VCH. (d) and (f) Reprinted from ref. 67 Copyright 2020, Wiley-VCH. (g) and (h) Reprinted from ref. 68 Copyright 2020, the American Chemical Society.

challenge.<sup>70</sup> Alternatively, the LPI-CVD method has the potential to overcome the difficulties of gas-phase control based solid powder and provides a new pathway. The liquid precursor allows precise control of the doping concentration<sup>71</sup> and enables uniform mixing of the dopant at the molecular level in the precursor solution, which in turn can be uniformly doped into 2D TMDs. Besides, it results in minimal contamination to the reaction chamber,<sup>72</sup> eliminating the influence of circulation residue.

In this section, we summarize the recent advances of atomic doping of 2D TMD monolayer by the LPI-CVD method.

### 3.1 Regulation of the electrical properties of 2D TMDs

Substitutional doping, where metal cations are replaced by directly introducing different conducting foreign metal atoms, can modulate the electrical properties of TMDs. In the case of the LPI-CVD method, the preparation of liquid-phase precursors plays an important role in precisely controlling the doping concentration, which can be controlled by precisely controlling the concentration of the doping elements in solution to change the electrical properties of 2D TMD materials. In 2019, Qin *et al.* successfully obtained Nb-doped monolayer WS<sub>2</sub> with a transformation from n-type to p-type by tailoring the doping concentrations of Nb in the LPI-CVD method, whose doping concentrations could reach up to  $>10^{14} \text{ cm}^{-2}$  ( $>10\%$  Nb) in WS<sub>2</sub> monolayer.<sup>73</sup> The scanning transmission electron microscopy (STEM) image of WS<sub>2</sub> with 10.3% Nb doping displayed some darker dots, occupying the positions of the W atoms compared to that of the undoped WS<sub>2</sub> (Fig. 6(a) and (b)), which confirms that the Nb doping is

carried out randomly with *in situ* atom substitution. Notably, the undoped WS<sub>2</sub> FET exhibited distinct n-type behavior (Fig. 6(c)) and 10.3% Nb-doped WS<sub>2</sub> FET (Fig. 6(d)) showed a clear indication of hole doping, which proved that the Nb dopants were the ionized acceptors at room temperature. Compared to the Nb element, the V element, as the doping cation, can also adjust the electrical properties of WSe<sub>2</sub> monolayers by the LPI-CVD method.<sup>74</sup> In contrast to the bipolar transport characteristics exhibited in the WSe<sub>2</sub> monolayer, the V-WSe<sub>2</sub> monolayer threshold voltage shifted to a positive value and exhibited significant p-type transport characteristics (Fig. 6(e)) with an increase in the V-doping concentration from 1% to 10%, and the charge mobility as well as the hole density increased with an increase in the V-doping concentration. The current switching ratio of the V-WSe<sub>2</sub> monolayer was as high as  $10^5$  with an increase in the V doping concentration to 4% (Fig. 6(f)).

Besides Nb and V, other metal atoms such as Re and Fe can be effectively doped in monolayer 2D TMDs to tune their electrical properties.<sup>75–78</sup> The Re atom was doped in MoS<sub>2</sub> as an electron donor. As the Re doping concentration gradually increased to 25%, the conductivity increased significantly and the threshold voltage shifted sharply to a more negative gate bias, exhibiting n-type transport characteristics (Fig. 6(g)).<sup>75</sup> In addition to changing the type of transport properties of 2D TMDs, the introduction of suitable doping atoms in the host material can also improve the electrocatalytic properties of 2D TMDs. Furthermore, metal-atom-doped TMDs can generate additional active sites to regulate the bandgap, manipulating the electrical properties, such as carrier concentration and



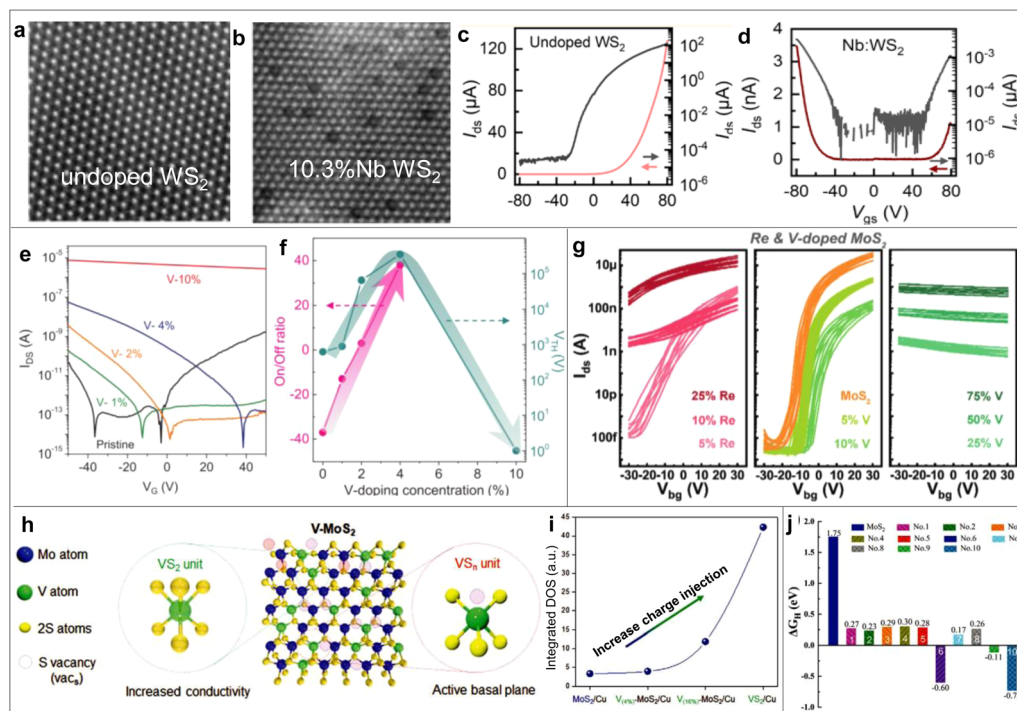


**Fig. 6** HAADF-STEM images of undoped (a) and 10.3% Nb-doped (b)  $\text{WS}_2$  flakes.<sup>73</sup> (c)  $I$ - $V$  curve of FET based on undoped  $\text{WS}_2$ .<sup>73</sup> (d)  $I$ - $V$  curve of FET based on 10.3% Nb-doped  $\text{WS}_2$ .<sup>73</sup> (e)  $I$ - $V$  curve of V-doped  $\text{WSe}_2$  transistors under  $V_{\text{DS}} = 0.5 \text{ V}$ .<sup>74</sup> (f) On/off ratio and threshold voltage as a function of V-doping concentration.<sup>74</sup> (g)  $I$ - $V$  curves of FETs based on Re-doped and V-doped TMDs.<sup>75</sup> (h) Illustration of V-MoS<sub>2</sub> with VS<sub>2</sub> and VS<sub>n</sub> units.<sup>77</sup> (i) Integrated density of states plots for MoS<sub>2</sub> at different V-doping.<sup>77</sup> (j) Hydrogen adsorption free energy for different defect configurations.<sup>78</sup> (a)–(d) Reprinted from ref. 73 Copyright 2019, the American Chemical Society. (e) and (f) Reprinted from ref. 74 Copyright 2019, Wiley-VCH. (g) Reprinted from ref. 75 Copyright 2021, Wiley-VCH. (h)–(i) Reprinted from ref. 77 Copyright 2021, Wiley-VCH. (j) Reprinted from ref. 78 Copyright 2022, Wiley-VCH.

mobility, which ultimately enhance the hydrogen evolution reaction (HER) catalytic activity. In 2021, Agyapong-Fordjour *et al.* doped V atoms into semiconducting MoS<sub>2</sub> to form nanodispersed metallic vanadium sulfide units *via* a one-step LPI-CVD method,<sup>77</sup> and the resulting V-doped MoS<sub>2</sub> exhibited excellent HER catalytic activity. During the growth process, the Mo atoms were replaced by V atoms to form VS<sub>2</sub> groups to enhance the electrical conductivity of V-doped MoS<sub>2</sub> materials, while V vacancies were created to form VS<sub>n</sub> groups to introduce additional active sites in the less reactive substrate planes of the MoS<sub>2</sub> materials to enhance the adsorption hydrogen (Fig. 6(h)). The DFT calculations yielded a Gibbs free energy of  $-0.02 \text{ eV}$  for VS<sub>n</sub> groups in V-MoS<sub>2</sub> monolayers on copper substrates, which is almost close to  $0 \text{ eV}$ . This indicates that the V-MoS<sub>2</sub> monolayer containing VS<sub>n</sub> groups has excellent catalytic properties for the HER. In addition, the density of states near the Fermi energy level associated with the active site increases with an increase in V-doping concentration (Fig. 6(i)), which illustrates the increase in the charge transfer rate of V-MoS<sub>2</sub>, ultimately yielding catalytic properties almost comparable to that of the Pt metal. Similarly, Liu *et al.* achieved the *in situ* doping of V atoms in MoS<sub>2</sub> monolayers *via* the LPI-CVD method with the lowest hydrogen adsorption free energy at the defective configuration of three V-doped atoms and S vacancies (Fig. 6(j)), which synergistically improved the catalytic performance of V-MoS<sub>2</sub> monolayers for the HER.<sup>78</sup> Therefore, the

LPI-CVD method offers significant advantages for *in situ* doping with precisely controlled doping concentrations, in which Mo or W can be replaced by an electron donor and acceptor, leading to a change in electronic structure, carrier types, and conductivity of TMD monolayers. We can envisage the extension of this approach to the introduction of a variety of other doping elements, making it possible to systematically study the fantastic modulation of various electrical properties.

### 3.2 Regulation of the optical properties of 2D TMDs

Due to their similar atomic structure, the doping concentration of 2D TMD materials can be varied over the entire composition range, thus modulating the energy band structure of 2D TMD materials. An outstanding advantage of the LPI-CVD method over the commonly used CVD preparation methods is the avoidance of inhomogeneous precursor vapor pressure generation. In 2019, Lee *et al.* successfully achieved the growth of Mo<sub>1-x</sub>W<sub>x</sub>S<sub>2</sub> monolayer with controlled composition by adjusting the ratio of MoO<sub>3</sub> and WO<sub>3</sub> using the LPI-CVD method.<sup>79</sup> The synthesized Mo<sub>1-x</sub>W<sub>x</sub>S<sub>2</sub> monolayer had a homogeneous chemical composition. The resulting PL mapping at  $1.90 \text{ eV}$  showed that the Mo<sub>1-x</sub>W<sub>x</sub>S<sub>2</sub> monolayers possessed a uniform chemical composition and structural characteristics (Fig. 7(a)). With an increase in the W composition ratio, the PL of the Mo<sub>1-x</sub>W<sub>x</sub>S<sub>2</sub> monolayers was blue-shifted (Fig. 7(b)). The variation in free excitons in the Mo<sub>1-x</sub>W<sub>x</sub>S<sub>2</sub>



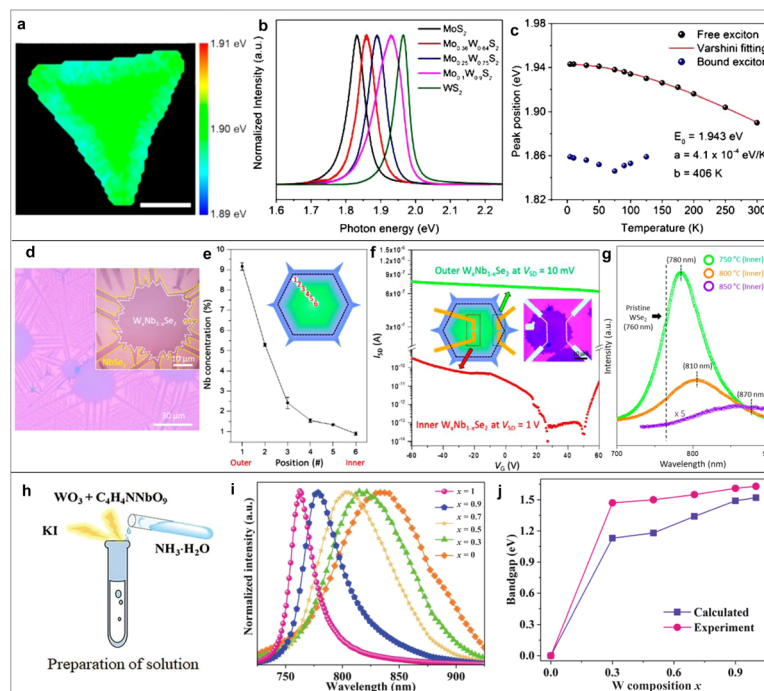


**Fig. 7** (a) PL position mapping of  $\text{Mo}_{1-x}\text{W}_x\text{S}_2$ .<sup>79</sup> (b) PL spectrum of  $\text{Mo}_{1-x}\text{W}_x\text{S}_2$ .<sup>79</sup> (c) Curves of peak position of the free excitons and the bound excitons with temperature.<sup>79</sup> (d) Optical image of the  $\text{NbSe}_2/\text{W}_x\text{Nb}_{1-x}\text{Se}_2$  heterostructure.<sup>60</sup> (e) Variation curve of Nb doping concentration with position from edge to inside.<sup>60</sup> (f)  $I$ - $V$  curve of the outer and the inner  $\text{W}_x\text{Nb}_{1-x}\text{Se}_2$  FET, where the insets show a schematic and optical images of the device.<sup>60</sup> (g) PL spectra of the inner  $\text{W}_x\text{Nb}_{1-x}\text{Se}_2$  region at different temperatures.<sup>60</sup> (h) Process for the preparation process of precursor solution.<sup>39</sup> (i) PL intensity of  $\text{Nb}_{1-x}\text{W}_x\text{Se}_2$  alloys with different W compositions.<sup>39</sup> (j) Curves of band gap variation with the ratio of W components.<sup>39</sup> (a)–(c) Reprinted from ref. 79 Copyright 2019, the American Chemical Society. (d)–(g) Reprinted from ref. 60 Copyright 2020, the American Chemical Society. (h)–(j) Reprinted from ref. 39 Copyright 2022, Springer Nature.

monolayer with temperature agrees well with the Varshni equation, while the bound excitons produce a turning point at 75 K (Fig. 7(c)).

Polygonal  $\text{W}_x\text{Nb}_{1-x}\text{Se}_2$  domains around 40  $\mu\text{m}$  were successfully synthesized using the LPI-CVD method, which possessed a heterogeneous structure with the outer sea urchin-like  $\text{NbSe}_2$  domains (Fig. 7(d)–(g)).<sup>60</sup> The emission peak of the PL spectrum of the internal  $\text{W}_x\text{Nb}_{1-x}\text{Se}_2$  redshifted to  $\sim 780$  nm (Fig. 7(g)) compared to that of pure  $\text{WSe}_2$ . In addition, the Nb atoms act as electron acceptors equivalent to p-type doping. The Fermi energy level moved below the valence band maximum as the proportion of Nb component increased, and the normalized PL peak position shifted continuously from 760 nm to 845 nm, which indicates that the energy band gap of the synthesized monolayer decreased continuously from 1.63 eV to 1.47 eV (Fig. 7(h)–(j)).<sup>39</sup> Therefore, the LPI-CVD method is a concise and effective approach for the preparation of alloys with continuously tunable band gaps. However, whether the universal preparation of multiple types of alloys can be achieved requires more efforts in the future.

### 3.3 Regulation of the magnetic properties of 2D TMDs

Materials with both ferromagnetic and semiconducting properties are called dilute magnetic semiconductors, which have great potential applications in spintronics and magnetoelectrics.<sup>80,81</sup> The doping of magnetic atoms such as Fe, Co, Ni, Mn, and V will produce ferromagnetism in non-ferromagnetic 2D TMDs.<sup>82–84</sup> Thus, the LPI-CVD method has become one of the most effective

methods for the controllable synthesis of substitutional magnetic transition metal-doped atomically thin TMDs. In 2020, Zhang *et al.* successfully synthesized high-quality V-doped monolayers of  $\text{WSe}_2$  with a wide range of V concentrations from 0 to 12% *via* the LPI-CVD method (Fig. 8(a) and (b)), which exhibited ferromagnetism at room temperature.<sup>85</sup> The ferromagnetism of the V-doped  $\text{WSe}_2$  increased with an increase in V concentration, and the maximum coercivity and saturation magnetization of the V-doped  $\text{WSe}_2$  was obtained when the V doping concentration reached 2% (Fig. 8(c)–(e)).

V doping produces a more pronounced change in the magnetic properties of  $\text{WSe}_2$  materials compared to that of V-doped  $\text{WS}_2$ . For example, Yun *et al.* reported that V-doped  $\text{WSe}_2$  possessed long-range ordered ferromagnetic domains at room-temperature (Fig. 8(f)).<sup>86</sup> The V- $\text{WSe}_2$  monolayer exhibited striped magnetic domains at a V doping concentration of 0.1% according to magnetic force microscopy (MFM) tests (Fig. 8(g)). As the doping concentration increased to 5%, the stripe-like domains of the V- $\text{WSe}_2$  monolayer clearly changed to polygonal shape and the domain area gradually decreases (Fig. 8(h)). The MFM phase test of 0.1% V- $\text{WSe}_2$  at different gate voltages showed that at a gate voltage of  $-10$  V, 0.1% V- $\text{WSe}_2$  had almost no magnetic domains (Fig. 8(i)). With a positive shift in the gate voltage to 20 V, domains gradually appeared with stripes, which indicates that the domains of the 0.1% V- $\text{WSe}_2$  monolayer can be regulated by the gate and the 0.1% V- $\text{WSe}_2$  monolayer is a dilute



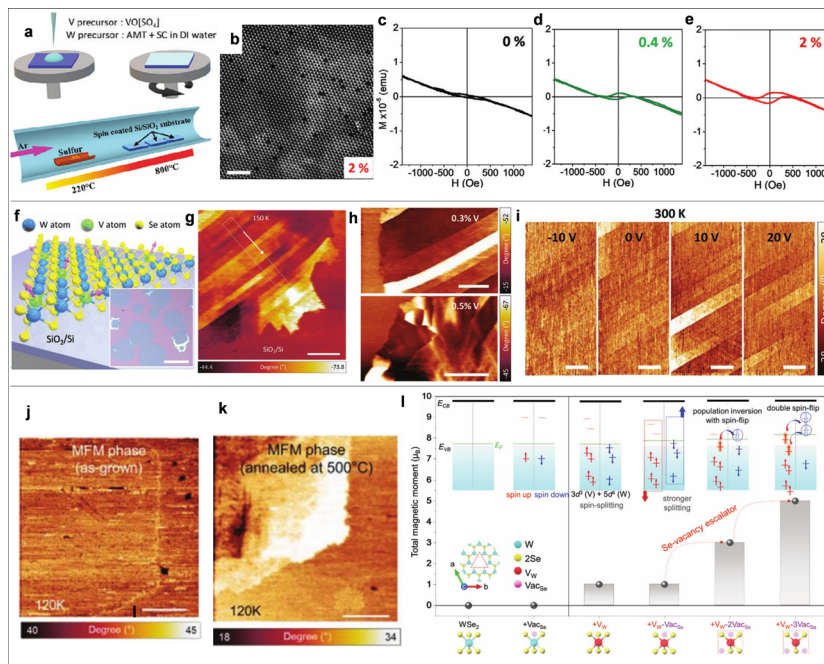


**Fig. 8** (a) Schematic of the synthesis of Fe-doped  $\text{MoSe}_2$ .<sup>85</sup> (b) HAADF-STEM images of V-doped  $\text{MoSe}_2$  at 2% concentration.<sup>85</sup> (c)–(e) Magnetization versus field loops for pristine (c) and V-doped  $\text{WS}_2$  at 0.4% (d) and 2% (e) concentration.<sup>85</sup> (f) Synthetic schematic of V-doped  $\text{WSe}_2$ , where the inset shows the optical image of V-doped  $\text{WSe}_2$ .<sup>86</sup> (g)–(h) MFM images of the magnetic domains of V-doped  $\text{WSe}_2$  with 0.1% (g) and 0.3% and 0.5% (h) concentrations.<sup>86</sup> (i) Gate-dependent MFM images for 0.1% V-doped  $\text{WSe}_2$ .<sup>86</sup> (j)–(k) MFM phase images measured at 120 K in as-grown (j) and annealed (k) V-doped  $\text{WSe}_2$ .<sup>40</sup> (l) Image of the variation in the total magnetic moment by DFT for different doping and vacancy binding types.<sup>40</sup> (a)–(e) Reprinted from ref. 85 Copyright 2020, Wiley-VCH. (f)–(i) Reprinted from ref. 86 Copyright 2020, Wiley-VCH. (j)–(l) Reprinted from ref. 40 Copyright 2022, Wiley-VCH.

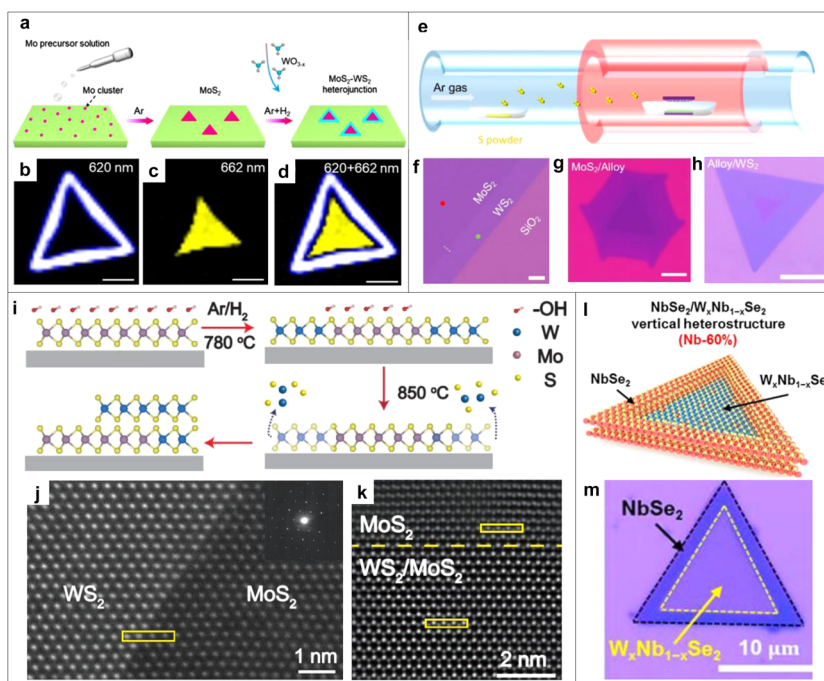


**Fig. 9** (a) Synthetic schematic of  $\text{MoS}_2/\text{WS}_2$  lateral heterostructures.<sup>89</sup> (b)–(d) PL intensity mapping of  $\text{MoS}_2/\text{WS}_2$  lateral heterostructures.<sup>89</sup> (e) Synthetic schematic of heterostructures and alloy.<sup>79</sup> (f)–(h) Optical images between  $\text{MoS}_2/\text{WS}_2$  (f),  $\text{MoS}_2/\text{alloy}$  (g),  $\text{alloy}/\text{WS}_2$  (h) and lateral heterostructures interfaces.<sup>79</sup> (i) Schematic of selective growth of  $\text{WS}_2/\text{MoS}_2$  lateral and vertical heterostructures.<sup>91</sup> (j) HAADF-STEM image of  $\text{WS}_2/\text{MoS}_2$  lateral heterostructures.<sup>91</sup> (k) HAADF-STEM image of  $\text{WS}_2/\text{MoS}_2$  vertical heterostructures.<sup>91</sup> (l) Atomic structure model of  $\text{NbSe}_2/\text{W}_x\text{Nb}_{1-x}\text{Se}_2$  vdWHs with 60% concentration.<sup>93</sup> (m) Optical microscopy of  $\text{NbSe}_2/\text{W}_x\text{Nb}_{1-x}\text{Se}_2$  vdWHs with 60% concentration.<sup>93</sup> (a)–(d) Reprinted from ref. 89 Copyright 2021, the American Chemical Society. (e)–(h) Reprinted from ref. 79 Copyright 2019, the American Chemical Society. (i)–(k) Reprinted from ref. 91 Copyright 2020, the American Chemical Society. (l)–(m) Reprinted from ref. 93 Copyright 2021, the American Chemical Society.



Table 1 Periodic table of soluble salts for the synthesis of 2D TMDs

IVB	VB	VIB	VIIIB	VIIIB	IB	IIIA	IVA	VA	VIA
$^{22}\text{Ti}$ ( $d^2s^2$ )	$^{23}\text{V}$ ( $d^3s^2$ )	$^{24}\text{Cr}$ ( $d^5s^1$ )	$^{26}\text{Fe}$ ( $d^6s^2$ )	$^{27}\text{Co}$ ( $d^7s^2$ )	$^{28}\text{Ni}$ ( $d^8s^2$ )	$^{31}\text{Ga}$ ( $s^2p^1$ )	$^{32}\text{Ge}$ ( $s^2p^2$ )		$^{16}\text{S}$ ( $s^2p^4$ )
$\text{TiOSO}_4$	$\text{VOSO}_4 \cdot x\text{H}_2\text{O}$	$\text{Na}_2\text{CrO}_4$	$\text{C}_6\text{H}_{12}\text{FeN}_3\text{O}_{12} \cdot 3\text{H}_2\text{O}$	$\text{Co}(\text{NH}_4)_2\text{SO}_4 \cdot x\text{H}_2\text{O}$	$\text{NiC}_4\text{H}_6\text{O}_4 \cdot 4\text{H}_2\text{O}$	$\text{Cu}(\text{NO}_3)_2$	$\text{Ge}(\text{OH})_4$		$(\text{NH})_2\text{SO}_4$
$\text{C}_4\text{K}_2\text{O}_9\text{Ti} \cdot 2\text{H}_2\text{O}$	$\text{NH}_4\text{VO}_3$			$\text{C}_4\text{H}_6\text{CoO}_4 \cdot 4\text{H}_2\text{O}$	$\text{Ni}(\text{SO}_3\text{NH}_2)_2 \cdot 4\text{H}_2\text{O}$	$\text{Cu}(\text{ClO}_3)_2$			
$^{40}\text{Zr}$ ( $d^2s^2$ )	$\text{NaVO}_3$	$^{42}\text{Mo}$ ( $d^5s^1$ )			$^{46}\text{Pd}$ ( $d^{10}$ )	$^{49}\text{In}$ ( $s^2p^1$ )	$^{50}\text{Sn}$ ( $s^2p^2$ )	$^{51}\text{Sb}$ ( $s^2p^3$ )	$^{34}\text{Se}$ ( $s^2p^4$ )
	$^{41}\text{Nb}$ ( $d^4s^1$ )	$\text{H}_{24}\text{Mo}_7\text{N}_6\text{O}_{24} \cdot 4\text{H}_2\text{O}$			$\text{Pd}(\text{C}_2\text{H}_3\text{O}_2)_2$	$\text{InBr}_3$	$\text{SnF}_2$	$\text{SbF}_3$	$\text{Na}_2\text{SeO}_3$
$\text{Zr}(\text{SO}_4)_2 \cdot 4\text{H}_2\text{O}$	$\text{C}_{10}\text{H}_5\text{NbO}_{20} \cdot x\text{H}_2\text{O}$	$\text{Na}_2\text{Mo}_2\text{O}_7$			$\text{Pd}(\text{NO}_3)_2$	$\text{InCl}_3$	$\text{SnSO}_4$	$\text{SbCl}_3$	
	$\text{C}_4\text{H}_4\text{NNbO}_9 \cdot n\text{H}_2\text{O}$	$\text{Na}_2\text{MoO}_4$							
	$\text{Nb}(\text{HC}_2\text{O}_4)_5$	$\text{K}_2\text{MoS}_4$							
		$(\text{NH}_4)_6\text{Mo}_7\text{O}_{24} \cdot 4\text{H}_2\text{O}$							
$^{72}\text{Hf}$ ( $d^2s^2$ )	$^{73}\text{Ta}$ ( $d^3s^2$ )	$^{74}\text{W}$ ( $d^4s^2$ )	$^{75}\text{Re}$ ( $d^5s^2$ )		$^{78}\text{Pt}$ ( $d^9s^1$ )			$^{83}\text{Bi}$ ( $s^2p^3$ )	$^{52}\text{Te}$ ( $s^2p^4$ )
					$\text{H}_2\text{PtCl}_6$			$\text{BiI}_3$	$\text{Na}_2\text{TeO}_3$
$\text{Hf}(\text{OH})_3$	$\text{TaCl}_5$	$\text{Na}_2\text{WO}_4$	$\text{NaReO}_4$					$\text{Bi}(\text{OH})_3$	
		$\text{Na}_2\text{W}_4\text{O}_{13}$						$\text{Bi}(\text{NO}_3)_3 \cdot 5\text{H}_2\text{O}$	
		$(\text{NH}_4)_{10}\text{W}_{12}\text{O}_{41}$							
		$(\text{NH}_4)_6\text{W}_{12}\text{O}_{39} \cdot 2\text{H}_2\text{O}$							

magnetic semiconductor. Recently, the ferromagnetic order of V-doped  $\text{WSe}_2$  synthesized by the LPI-CVD method was enhanced through post-annealing treatment.<sup>40</sup> Compared to the unannealed V- $\text{WSe}_2$  monolayers, the V- $\text{WSe}_2$  monolayers clearly produced polygonal-shaped magnetic domains after annealing at 500 °C (Fig. 8(j) and (k)). Before annealing, the doping of the V atom caused spin splitting, and the hybridization of the V-3d and W-5d orbitals produced emerging defect states, which increased the magnetic moment of V- $\text{WSe}_2$  by 1  $\mu_B$ , while the paired configuration of  $\text{V}_W\text{-Vac}_{\text{Se}}$  after annealing intensified the spin splitting (Fig. 8(l)), and the strong spin splitting caused by the formation of  $\text{V}_W\text{-2Vac}_{\text{Se}}$  with an increase in the concentration of sulfur vacancies caused population inversion. Additionally, the magnetic moment increased to 3  $\mu_B$ , and in the  $\text{V}_W\text{-3Vac}_{\text{Se}}$  configuration, the magnetic moment increased to 5  $\mu_B$  to reach saturation. Except for V atoms, other magnetic atoms such as Fe, Co, and Ni can also dope the 2D TMDs and modulate the ferromagnetic properties of the materials.<sup>87</sup>

## 4. Heterostructures based on 2D TMDs

High-quality lateral heterostructures require atomic-level sharpness at the interface of different 2D materials.<sup>88</sup> Controlling the supply sequence of precursors, and thus the orderly growth of different materials in a heterojunction is an important idea for the synthesis of high-quality heterostructures in the LPI-CVD method. High-quality  $\text{MoS}_2/\text{WS}_2$  lateral heterostructures have been comprehensively reported using the LPI-CVD method.<sup>79,88,89</sup> For example, Chen *et al.* synthesized large-area  $\text{MoS}_2/\text{WS}_2$  lateral heterostructures using  $\text{H}_2$  as the reducing agent.<sup>89</sup> This chemical vapor deposition combined with hydrogen-triggered method could accurately control the precursor source supply period due to the different volatilities between feedstocks. During the growth process, the  $\text{MoS}_2$  monolayer was firstly grown due to the higher volatility of the Mo source compared to  $\text{WO}_3$  under Ar gas, followed by the reduction of  $\text{WO}_3$  to highly volatile  $\text{WO}_{3-x}$  after the introduction of  $\text{H}_2$ , and  $\text{WS}_2$  started to grow seamlessly around  $\text{MoS}_2$ , forming a high-quality  $\text{MoS}_2/\text{WS}_2$  lateral heterostructure (Fig. 9(a)). It is clear that the  $\text{MoS}_2/\text{WS}_2$  lateral heterostructure consisted of seamlessly stitched  $\text{MoS}_2$  and  $\text{WS}_2$  regions with atomically sharp interfaces (Fig. 9(b)–(d)). Controlling the supply sequence of different precursor sources by using the difference in the volatility of precursor raw materials is one of the common methods for growing heterostructures currently; however, controlling the key parameters in CVD growth is equally important for the synthesis of heterostructure. Consequently, lateral heterostructures ( $\text{MoS}_2/\text{WS}_2$ ,  $\text{MoS}_2/\text{alloy}$ , and  $\text{alloy}/\text{WS}_2$ ) have been successfully synthesized by precisely controlling key factors such as the relative supersaturation degree of the precursor, the sulfur vaporization temperature, and the growth temperature (Fig. 9(e)–(h)).<sup>79</sup> Depending on the physical or chemical properties of the precursor source, the order of precursor supply is regulated by strictly controlling the growth temperature to selectively grow high-quality lateral/vertical heterostructures.<sup>90</sup> In the LPI-CVD method, the growth temperature can regulate the adsorption or dissociation state of  $\text{OH}^-$  ions on



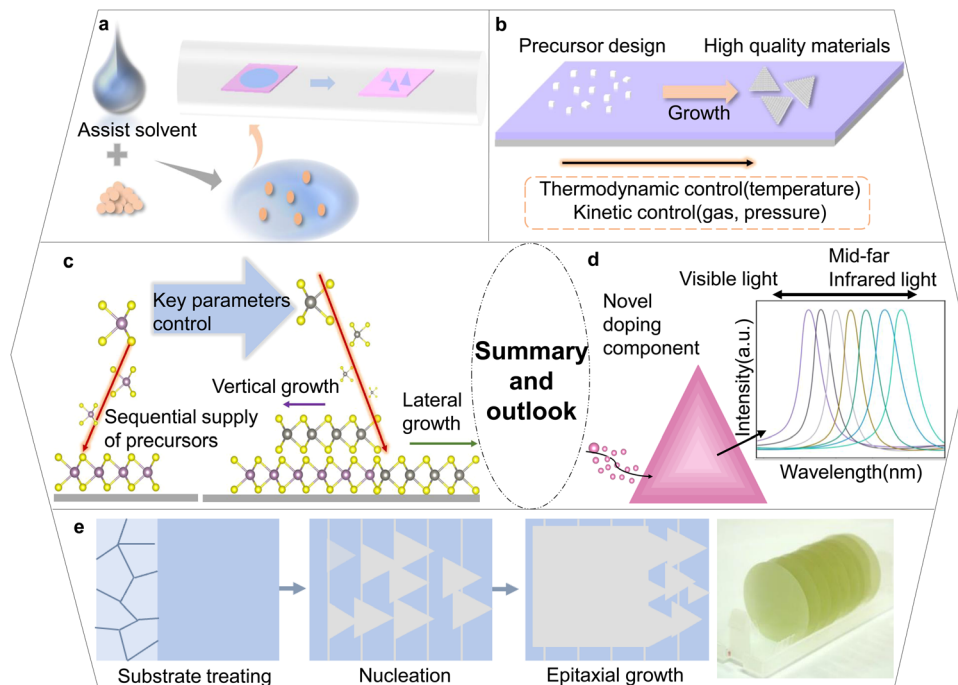


**Fig. 10** (a) Growth process using other assistant solvents or promoters. (b) Application of precursor design and multi-condition to regulate the growth process. (c) Control of key parameters regulating the sequential supply of precursors and selection for the growth of vertical or lateral heterostructures. (d) Doping with other novel elements to modulate the alloy band gap from visible to mid- and far-infrared light range. (e) Pre-treating substrates to control domain unidirectional growth and seamlessly stitch together wafer-scale monolayer films. (e) Reprinted from ref. 96 Copyright 2017, the American Chemical Society.

the monolayer  $\text{MoS}_2$  surface.<sup>91</sup> When the growth temperature reached 780 °C (Fig. 9(i)),  $\text{OH}^-$  ions were fully adsorbed on the surface of the monolayer  $\text{MoS}_2$ , and the formed  $\text{OH}^-$  ion layer passivated the  $\text{MoS}_2$  surface, preventing the W atoms from nucleating on the  $\text{MoS}_2$  surface for vertical growth, and eventually, the W atoms nucleated at the edge of  $\text{MoS}_2$  to form the  $\text{WS}_2/\text{MoS}_2$  lateral heterostructure with atomically sharp interfaces (Fig. 9(j)). As the temperature increased, the  $\text{OH}^-$  ions dissociated from the surface of monolayer  $\text{MoS}_2$ , leading to the exposure of surface of monolayer  $\text{MoS}_2$ . To reduce the total energy of the  $\text{WS}_2/\text{MoS}_2$  heterostructure,  $\text{WS}_2$  preferentially nucleated on the surface of  $\text{MoS}_2$ , resulting in high-quality  $\text{WS}_2/\text{MoS}_2$  vertical heterostructure (Fig. 9(k)).

Changing the growth temperature can affect the thermodynamic tendency of growth during the synthesis of heterostructures, for example, Bai *et al.* reported a two-step heating process to grow  $\text{MoS}_2$  monolayers at lower temperatures, while growing  $\text{WS}_2$  monolayers on the surface of  $\text{MoS}_2$  at high temperatures due to the large energy potential barrier by the LPI-CVD method, resulting in the formation of stable  $\text{MoS}_2/\text{WS}_2$  vertical heterostructures with an orientation difference of 60°. <sup>92</sup> Recently,  $\text{NbSe}_2/\text{W}_x\text{Nb}_{1-x}\text{Se}_2$  van der Waals vertical heterostructures (vdWHs) were synthesized using a one-step LPI-CVD growth method.<sup>93</sup> As the temperature increased, the Nb precursor evaporated and absorbed enough energy to overcome the substrate surface energy barrier, preferentially nucleating the growth at the edge of the monolayer Nb-doped  $\text{WSe}_2$  (Fig. 9(l)), followed by extension to the middle part, and finally completing coverage to achieve the growth of

$\text{NbSe}_2/\text{W}_x\text{Nb}_{1-x}\text{Se}_2$  van der Waals vertical heterostructures, and the optical images are shown in Fig. 9(m). Notably, the energy band structure of the constructed vertical/lateral heterostructures can be modulated by changing the type of 2D materials, and thus the electrical properties of the constructed electronic devices. To expand the application of these materials in electronic and optoelectronic electronic devices, more efforts are needed to develop more generalized LPI-CVD methods for the synthesis of heterostructures.<sup>70,94</sup>

## 5. Summary and outlook

In this review, we mainly overviewed the recent research on the LPI-CVD growth of 2D TMDs, including monolayer 2D TMDs, with doping and heterostructures. The precursor solution in the LPI-CVD process enables the homogeneous mixing of multiple precursors at the molecular level to facilitate the growth of wafer-scale 2D TMDs.<sup>95</sup> For the controllable growth of larger area and higher quality TMDs with more excellent physical performance, various assisted treatments based on LPI-CVD strategies were implemented mainly including molten-salt assisted, hydroxide-assisted, polymer-assisted, and supply of novel chalcogen precursor LPI-CVD. In addition, the recent progress of atomically doped monolayer 2D TMDs was summarized. Furthermore, we further elaborated the latest progress on the growth of heterostructures based on LPI-CVD. Notably, although the LPI-CVD method has shown great



potential for the high-quality growth of atomically thin 2D TMDs, doped 2D TMDs and heterostructures, the growth of 2D TMDs *via* LPI-CVD is still in infancy and faces some challenges, as follows:

(I) At present, in the huge TMD family, only a small number of TMDs such as  $\text{MoS}_2$ ,  $\text{MoSe}_2$ , and  $\text{WSe}_2$  has been successfully grown in high quality by the LPI-CVD method. However, the LPI-CVD method is strongly dependent on the precursor salts of each element, as shown in the Table 1, which can be used as precursors to grow more 2D TMDs. Therefore, more efforts need to be devoted to finding various assisted treatments such as organic solvents (Fig. 10(a)) and other co-solvents to promote the dissolution and reaction of salts for the growth of more 2D TMDs.

(II) The quality of 2D TMDs obtained by LPI-CVD growth is still inferior compared to that produced by mechanical exfoliation. For example, excessive or insufficient spin coating of the precursor solutions can lead to a dense nucleation density or insufficient source supply during growth, producing unavoidable defects. Therefore, more precise precursor design (Fig. 10(b)) and the reaction processes of serial reactions should be drastically implemented to improve the high-quality growth of 2D TMDs.

(III) The mechanism of controlled lateral/vertical heterostructure growth remains unclear, although that produced by LPI-CVD methods is advantageous. The regulation of key parameters such as the growth temperature and gas flow during growth is essentially the regulation of the growth thermodynamics and growth kinetic competition between the precursor materials. The intrinsic growth mechanism (Fig. 10(c)) should be understood in depth to develop new synthetic methods that can precisely control the order of precursor introduction to achieve the growth of multiple high-quality lateral heterostructures.

(IV) Controllable doping of 2D TMDs still needs further exploration. Although controllable doping such as  $\text{W}_x\text{Nb}_{1-x}\text{Se}_2$  can effectively regulate the electrical and optical properties of TMDs, the range of band gap regulation is limited such as 1.47–1.63 eV. The LPI-CVD method plays an important role in growing doped 2D TMDs, and therefore exploring novel doping components (such as Re, In, and Te) for the LPI-CVD method is urgently required to control the growth of lateral composition-graded atomic-layered 2D TMD nanosheets with tunable bandgaps from the visible to mid-to-far infrared range (Fig. 10(d)).

(V) The growth of large-area continuity, large domain size, and thickness uniformity 2D semiconductors, as the prerequisite of industrial optoelectronic integration application, is still very challenging.<sup>96</sup> Although the LPI-CVD method has great potential for the growth of 2D TMDs, the preparation of wafer-scale size especially large single crystals of 2D TMDs still in its infancy. Therefore, given the centimeter-scale epitaxy of graphene and  $\text{MoS}_2$  on annealed copper foil or sapphire, searching for substrates designed for good contact with the precursor solutions, and annealing or other treatment can enable the seamless stitching of unidirectionally aligned domains into wafer-scale single-crystal films (Fig. 10(e)) by suppressing the nucleation rate and edge induction as a path worth exploring.

## Conflicts of interest

There are no conflicts to declare.

## Acknowledgements

This work was supported by the National Key Research and Development Program of China (2021YFA1200700), the National Natural Science Foundation of China (62225404, 61927808, 62174026, 6507024076), and the Strategic Priority Research Program of Chinese Academy of Sciences (XDB30000000).

## Notes and references

- 1 Z. Wang, H.-H. Wu, Q. Li, F. Besenbacher, X. C. Zeng and M. Dong, *Nanoscale*, 2018, **10**, 18178–18185.
- 2 Z. Wang, H.-H. Wu, Q. Li, F. Besenbacher, Y. Li, X. C. Zeng and M. Dong, *Adv. Sci.*, 2020, **7**, 1901382.
- 3 Z. Hu, X. Kuai, J. Chen, P. Sun, Q. Zhang, H.-H. Wu and L. Zhang, *ChemSusChem*, 2020, **13**, 1485–1490.
- 4 K. S. Novoselov, A. K. Geim, S. V. Morozov, D. Jiang, Y. Zhang, S. V. Dubonos, I. V. Grigorieva and A. A. Firsov, *Science*, 2004, **306**, 666–669.
- 5 H. J. Conley, B. Wang, J. I. Ziegler, R. F. Haglund, Jr., S. T. Pantelides and K. I. Bolotin, *Nano Lett.*, 2013, **13**, 3626–3630.
- 6 S. Mouri, Y. Miyauchi and K. Matsuda, *Nano Lett.*, 2013, **13**, 5944–5948.
- 7 I. Datta, S. H. Chae, G. R. Bhatt, M. A. Tadayon, B. Li, Y. Yu, C. Park, J. Park, L. Cao, D. N. Basov, J. Hone and M. Lipson, *Nat. Photonics*, 2020, **14**, 256–262.
- 8 S. B. Desai, S. R. Madhvapathy, A. B. Sachid, J. P. Llinas, Q. Wang, G. H. Ahn, G. Pitner, M. J. Kim, J. Bokor and C. Hu, *Science*, 2016, **354**, 99.
- 9 Y. Zhang, Y.-W. Tan, H. L. Stormer and P. Kim, *Nature*, 2005, **438**, 201–204.
- 10 Q. Li, X. Zhao, L. Deng, Z. Shi, S. Liu, Q. Wei, L. Zhang, Y. Cheng, L. Zhang, H. Lu, W. Gao, W. Huang, C. W. Qiu, G. Xiang, S. J. Pennycook, Q. Xiong, K. P. Loh and B. Peng, *ACS Nano*, 2020, **14**, 4636–4645.
- 11 B. Zhao, Z. Wan, Y. Liu, J. Xu, X. Yang, D. Shen, Z. Zhang, C. Guo, Q. Qian, J. Li, R. Wu, Z. Lin, X. Yan, B. Li, Z. Zhang, H. Ma, B. Li, X. Chen, Y. Qiao, I. Shakir, Z. Almutairi, F. Wei, Y. Zhang, X. Pan, Y. Huang, Y. Ping, X. Duan and X. Duan, *Nature*, 2021, **591**, 385–390.
- 12 S. B. Desai, G. Seol, J. S. Kang, H. Fang, C. Battaglia, R. Kapadia, J. W. Ager, J. Guo and A. Javey, *Nano Lett.*, 2014, **14**, 4592–4597.
- 13 J. Xia, X. Huang, L. Z. Liu, M. Wang, L. Wang, B. Huang, D. D. Zhu, J. J. Li, C. Z. Gu and X. M. Meng, *Nanoscale*, 2014, **6**, 8949–8955.
- 14 X. Chen, Y. Qiu, G. Liu, W. Zheng, W. Feng, F. Gao, W. Cao, Y. Fu, W. Hu and P. Hu, *J. Mater. Chem. A*, 2017, **5**, 11357–11363.
- 15 C. Xie, C. Mak, X. Tao and F. Yan, *Adv. Funct. Mater.*, 2017, **27**, 1603886.



- 16 S. Y. Wang, T. S. Ko, C. C. Huang, D. Y. Lin and Y. S. Huang, *Jpn. J. Appl. Phys.*, 2014, **53**, 04EH07.
- 17 X. Lin, W. Yang, K. L. Wang and W. Zhao, *Nat. Electron.*, 2019, **2**, 274–283.
- 18 W. S. Yun and J. D. Lee, *Phys. Chem. Chem. Phys.*, 2014, **16**, 8990–8996.
- 19 B. Zhao, W. Dang, Y. Liu, B. Li, J. Li, J. Luo, Z. Zhang, R. Wu, H. Ma, G. Sun, Y. Huang, X. Duan and X. Duan, *J. Am. Chem. Soc.*, 2018, **140**, 14217–14223.
- 20 Z. Cai, B. Liu, X. Zou and H. M. Cheng, *Chem. Rev.*, 2018, **118**, 6091–6133.
- 21 C. H. Naylor, W. M. Parkin, J. Ping, Z. Gao and A. T. C. Johnson, *Nano Lett.*, 2016, **16**, 4297–4304.
- 22 X. Tong, K. Liu, M. Zeng and L. Fu, *InfoMat*, 2019, **1**, 460–478.
- 23 J. H. Lee, E. K. Lee, W. J. Joo, Y. Jang, B. S. Kim, J. Y. Lim, S. H. Choi, S. J. Ahn, J. R. Ahn, M. H. Park, C. W. Yang, B. L. Choi, S. W. Hwang and D. Whang, *Science*, 2014, **344**, 286–289.
- 24 T. Zhang and L. Fu, *Chem*, 2018, **4**, 671–689.
- 25 T. Li, W. Guo, L. Ma, W. Li, Z. Yu, Z. Han, S. Gao, L. Liu, D. Fan, Z. Wang, Y. Yang, W. Lin, Z. Luo, X. Chen, N. Dai, X. Tu, D. Pan, Y. Yao, P. Wang, Y. Nie, J. Wang, Y. Shi and X. Wang, *Nat. Nanotechnol.*, 2021, **16**, 1201–1207.
- 26 J. C. Shaw, H. Zhou, Y. Chen, N. O. Weiss, Y. Liu, Y. Huang and X. Duan, *Nano Res.*, 2015, **7**, 511–517.
- 27 S. H. Choi, S. Boandoh, Y. H. Lee, J. S. Lee, J. H. Park, S. M. Kim, W. Yang and K. K. Kim, *ACS Appl. Mater. Interfaces*, 2017, **9**, 43021–43029.
- 28 S. Li, *iScience*, 2021, **24**, 103229.
- 29 P. Braeuninger-Weimer, B. Brennan, A. J. Pollard and S. Hofmann, *Chem. Mater.*, 2016, **28**, 8905–8915.
- 30 P. Yang, S. Zhang, S. Pan, B. Tang, Y. Liang, X. Zhao, Z. Zhang, J. Shi, Y. Huan, Y. Shi, S. J. Pennycook, Z. Ren, G. Zhang, Q. Chen, X. Zou, Z. Liu and Y. Zhang, *ACS Nano*, 2020, **14**, 5036–5045.
- 31 C. Chang, W. Chen, Y. Chen, Y. H. Chen, Y. Chen, F. Ding, C. H. Fan, H. J. Fan, Z. X. Fan, C. Gong, Y. J. Gong, Q. Y. He, X. Hong, S. Hu, W. D. Hu, W. Huang, Y. Huang, W. Ji, D. H. Li, L. J. Li, Q. Li, L. Lin, C. Y. Ling, M. H. Liu, N. Liu, Z. Liu, K. P. Loh, J. M. Ma, F. Miao, H. L. Peng, M. F. Shao, L. Song, S. Su, S. Sun, C. L. Tan, Z. Y. Tang, D. S. Wang, H. Wang, J. L. Wang, X. Wang, X. R. Wang, A. T. S. Wee, Z. M. Wei, Y. E. Wu, Z. S. Wu, J. Xiong, Q. H. Xiong, W. G. Xu, P. Yin, H. B. Zeng, Z. Y. Zeng, T. Y. Zhai, H. Zhang, H. Zhang, Q. C. Zhang, T. R. Zhang, X. Zhang, L. D. Zhao, M. T. Zhao, W. J. Zhao, Y. X. Zhao, K. G. Zhou, X. Zhou, Y. Zhou, H. W. Zhu, H. Zhang and Z. F. Liu, *Acta. Phys.-Chim. Sin.*, 2021, **37**(12), 2108017.
- 32 T. Carey, S. Cacovich, G. Divitini, J. Ren, A. Mansouri, J. M. Kim, C. Wang, C. Ducati, R. Sordan and F. Torrisi, *Nat. Commun.*, 2017, **8**, 1202.
- 33 X. Gao, G. Bian and J. Zhu, *J. Mater. Chem. C*, 2019, **7**, 12835–12861.
- 34 Y. Jeon, J. Seo, J. Kim, D. Rhee, M. Jung, H. Park and J. Kang, *Adv. Opt. Mater.*, 2022, **10**, 2101492.
- 35 B. Zhao, D. Shen, Z. Zhang, P. Lu, M. Hossain, J. Li, B. Li and X. Duan, *Adv. Funct. Mater.*, 2021, **31**, 2105132.
- 36 H. Cun, M. Macha, H. Kim, K. Liu, Y. Zhao, T. LaGrange, A. Kis and A. Radenovic, *Nano Res.*, 2019, **12**, 2646–2652.
- 37 D. Zhang, C. Wen, J. B. McClimon, P. Masih Das, Q. Zhang, G. A. Leone, S. V. Mandyam, M. Drndić, A. T. C. Johnson and M. Q. Zhao, *Adv. Electron. Mater.*, 2021, **7**, 2001219.
- 38 H. Liu, G. Qi, C. Tang, M. Chen, Y. Chen, Z. Shu, H. Xiang, Y. Jin, S. Wang, H. Li, M. Ouzounian, T. S. Hu, H. Duan, S. Li, Z. Han and S. Liu, *ACS Appl. Mater. Interfaces*, 2020, **12**, 13174–13181.
- 39 B. An, Y. Ma, F. Chu, X. Li, Y. Wu, C. You, W. Deng, S. Li and Y. Zhang, *Nano Res.*, 2022, **15**, 2608–2615.
- 40 S. J. Yun, B. W. Cho, T. Dinesh, D. H. Yang, Y. I. Kim, J. W. Jin, S.-H. Yang, T. D. Nguyen, Y.-M. Kim, K. K. Kim, D. L. Duong, S.-G. Kim and Y. H. Lee, *Adv. Mater.*, 2022, **34**, 2106551.
- 41 S. Wang, Y. Zhang, D. Zhao, J. Li, H. Kang, S. Zhao, T. Jin, J. Zhang, Z. Xue, Y. Wang, Y. Sui, Z. Chen, S. Peng, Z. Jin, X. Liu, J. Wang, Y. Chen and G. Yu, *2D Mater.*, 2021, **9**, 015016.
- 42 O. Lopez-Sanchez, D. Lembke, M. Kayci, A. Radenovic and A. Kis, *Nat. Nanotechnol.*, 2013, **8**, 497–501.
- 43 Z. Yan, J. Lin, Z. W. Peng, Z. Z. Sun, Y. Zhu, L. Li, C. S. Xiang, E. L. Samuel, C. Kittrell and J. M. Tour, *ACS Nano*, 2013, **7**, 2872.
- 44 S. Li, S. Wang, D.-M. Tang, W. Zhao, H. Xu, L. Chu, Y. Bando, D. Golberg and G. Eda, *Appl. Mater. Today.*, 2015, **1**, 60–66.
- 45 U. G. Lee, W.-B. Kim, D. H. Han and H. S. Chung, *Symmetry*, 2019, **11**, 1183.
- 46 Y. Zuo, W. Yu, C. Liu, X. Cheng, R. Qiao, J. Liang, X. Zhou, J. Wang, M. Wu, Y. Zhao, P. Gao, S. Wu, Z. Sun, K. Liu, X. Bai and Z. Liu, *Nat. Nanotechnol.*, 2020, **15**, 987–991.
- 47 Q. Wang, N. Li, J. Tang, J. Zhu, Q. Zhang, Q. Jia, Y. Lu, Z. Wei, H. Yu, Y. Zhao, Y. Guo, L. Gu, G. Sun, W. Yang, R. Yang, D. Shi and G. Zhang, *Nano Lett.*, 2020, **20**, 7193–7199.
- 48 C. Song, G. Noh, T. S. Kim, M. Kang, H. Song, A. Ham, M.-K. Jo, S. Cho, H.-J. Chai, S. R. Cho, K. Cho, J. Park, S. Song, I. Song, S. Bang, J. Y. Kwak and K. Kang, *ACS Nano*, 2020, **14**, 16266–16300.
- 49 J. Wang, T. Li, Q. Wang, W. Wang, R. Shi, N. Wang, A. Amini and C. Cheng, *Mater. Today Adv.*, 2020, **8**, 100098.
- 50 K. K. Liu, W. Zhang, Y. H. Lee, Y. C. Lin, M. T. Chang, C. Y. Su, C. S. Chang, H. Li, Y. Shi, H. Zhang, C. S. Lai and L. J. Li, *Nano Lett.*, 2012, **12**, 1538–1544.
- 51 A. S. George, Z. Mutlu, R. Ionescu, R. J. Wu, J. S. Jeong, H. H. Bay, Y. Chai, K. A. Mkhoyan, M. Ozkan and C. S. Ozkan, *Adv. Funct. Mater.*, 2014, **24**, 7461–7466.
- 52 S. Li, Y. C. Lin, X. Y. Liu, Z. Hu, J. Wu, H. Nakajima, S. Liu, T. Okazaki, W. Chen, T. Minari, Y. Sakuma, K. Tsukagoshi, K. Suenaga, T. Taniguchi and M. Osada, *Nanoscale*, 2019, **11**, 16122–16129.
- 53 C. Zhang, J. Wu, Y. Sun, C. Tan, T. Li, T. Tu, Y. Zhang, Y. Liang, X. Zhou, P. Gao and H. Peng, *J. Am. Chem. Soc.*, 2020, **142**, 2726–2731.
- 54 X. Wan, X. Miao, J. Yao, S. Wang, F. Shao, S. Xiao, R. Zhan, K. Chen, X. Zeng, X. Gu and J. Xu, *Adv. Mater.*, 2021, **33**, e2100260.



- 55 Q. Ji, C. Su, N. Mao, X. Tian, J.-C. Idrobo, J. Miao, W. A. Tisdale, A. Zettl, J. Li and J. Kong, *Sci. Adv.*, 2021, **7**, eabj3274.
- 56 M. Kim, J. Seo, J. Kim, J. S. Moon and H. Park, *ACS Nano*, 2021, **15**, 3038–3046.
- 57 S. Li, Y.-C. Lin, J. Hong, B. Gao, H. Lim, X. Yang, S. Liu, Y. Tateyama, K. Tsukagoshi, Y. Sakuma, K. Suenaga and T. Taniguchi, *Chem. Mater.*, 2021, **33**, 7301–7308.
- 58 D. Jiang, X. Wang, R. Chen, J. Sun, H. Kang, D. Ji, Y. Liu and D. Wei, *J. Am. Chem. Soc.*, 2022, **144**, 8746–8755.
- 59 J. Zhu, H. Xu, G. Zou, W. Zhang, R. Chai, J. Choi, J. Wu, H. Liu, G. Shen and H. Fan, *J. Am. Chem. Soc.*, 2019, **141**, 5392–5401.
- 60 S. Park, S. J. Yun, Y. I. Kim, J. H. Kim, Y. M. Kim, K. K. Kim and Y. H. Lee, *ACS Nano*, 2020, **14**, 8784–8792.
- 61 L. Ma, J. Zhu, W. Li, R. Huang and G. Zou, *J. Am. Chem. Soc.*, 2021, **143**, 13314–13324.
- 62 J. Yang, Y. Gu, E. Lee, H. Lee, S. H. Park, M. H. Cho, Y. H. Kim, Y. H. Kim and H. Kim, *Nanoscale*, 2015, **7**, 9311–9319.
- 63 H. Yang, A. Giri, S. Moon, S. Shin, J.-M. Myoung and U. Jeong, *Chem. Mater.*, 2017, **29**, 5772–5776.
- 64 R. Ionescu, B. Campbell, R. Wu, E. Aytan, A. Patalano, I. Ruiz, S. W. Howell, A. E. McDonald, T. E. Beechem, K. A. Mkhoyan, M. Ozkan and C. S. Ozkan, *Sci. Rep.*, 2017, **7**, 6419.
- 65 J. Kim, H. Seung, D. Kang, J. Kim, H. Bae, H. Park, S. Kang, C. Choi, B. K. Choi, J. S. Kim, T. Hyeon, H. Lee, D. H. Kim, S. Shim and J. Park, *Nano Lett.*, 2021, **21**, 9153–9163.
- 66 S. Boandoh, S. H. Choi, J. H. Park, S. Y. Park, S. Bang, M. S. Jeong, J. S. Lee, H. J. Kim, W. Yang, J. Y. Choi, S. M. Kim and K. K. Kim, *Small*, 2017, **13**, 1701306.
- 67 S. Feng, J. Tan, S. Zhao, S. Zhang, U. Khan, L. Tang, X. Zou, J. Lin, H. M. Cheng and B. Liu, *Small*, 2020, **16**, 2003357.
- 68 Y. Jin, M. Cheng, H. Liu, M. Ouzounian, T. S. Hu, B. You, G. Shao, X. Liu, Y. Liu, H. Li, S. Li, J. Guan and S. Liu, *Chem. Mater.*, 2020, **32**, 5616–5625.
- 69 J. Seo, J. Lee, S. Baek, W. Jung, N. K. Oh, E. Son and H. Park, *ACS Appl. Electron. Mater.*, 2021, **3**, 5528–5536.
- 70 J. Zou, Z. Cai, Y. Lai, J. Tan, R. Zhang, S. Feng, G. Wang, J. Lin, B. Liu and H. M. Cheng, *ACS Nano*, 2021, **15**, 7340–7347.
- 71 J. Zhang, Y. Zhu, M. Tebyetekerwa, D. Li, D. Liu, W. Lei, L. Wang, Y. Zhang and Y. Lu, *ACS Appl. Nano. Mater.*, 2020, **4**, 769–777.
- 72 K. Zhang, B. M. Bersch, J. Joshi, R. Addou, C. R. Cormier, C. Zhang, K. Xu, N. C. Briggs, K. Wang, S. Subramanian, K. Cho, S. Fullerton-Shirey, R. M. Wallace, P. M. Vora and J. A. Robinson, *Adv. Funct. Mater.*, 2018, **28**, 1706950.
- 73 Z. Qin, L. Loh, J. Wang, X. Xu and G. Eda, *ACS Nano*, 2019, **13**, 10768–10775.
- 74 S. Fan, S. J. Yun, W. J. Yu and Y. H. Lee, *Adv. Sci.*, 2020, **7**, 1902751.
- 75 S. Li, J. Hong, B. Gao, Y. C. Lin, H. E. Lim, X. Lu, J. Wu, S. Liu, Y. Tateyama, Y. Sakuma, K. Tsukagoshi, K. Suenaga and T. Taniguchi, *Adv. Sci.*, 2021, **8**, e2004438.
- 76 T. Zhang, K. Fujisawa, F. Zhang, M. Liu, M. C. Lucking, R. N. Gontijo, Y. Lei, H. Liu, K. Crust, T. Granzier-Nakajima, H. Terrones, A. L. Elias and M. Terrones, *ACS Nano*, 2020, **14**, 4326–4335.
- 77 F. O. Agyapong-Fordjour, S. J. Yun, H. J. Kim, W. Choi, B. Kirubasankar, S. H. Choi, L. A. Adofo, S. Boandoh, Y. I. Kim, S. M. Kim, Y. M. Kim, Y. H. Lee, Y. K. Han and K. K. Kim, *Adv. Sci.*, 2021, **8**, e2003709.
- 78 X. Liu, X. Jiang, G. Shao, H. Xiang, Z. Li, Y. Jin, Y. Chen, H. Jiang, H. Li, J. Shui, Y. Feng and S. Liu, *Small*, 2022, **18**, 2200601.
- 79 J. Lee, S. Pak, Y. W. Lee, Y. Park, A. R. Jang, J. Hong, Y. Cho, B. Hou, S. Lee, H. Y. Jeong, H. S. Shin, S. M. Morris, S. Cha, J. I. Sohn and J. M. Kim, *ACS Nano*, 2019, **13**, 13047–13055.
- 80 L. Yang, H. Wu, L. Zhang, G. Zhang, H. Li, W. Jin, W. Zhang and H. Chang, *ACS Appl. Mater. Interfaces*, 2021, **13**, 31880–31890.
- 81 B. Li, T. Xing, M. Zhong, L. Huang, N. Lei, J. Zhang, J. Li and Z. Wei, *Nat. Commun.*, 2017, **8**, 1958.
- 82 L. Yang, H. Wu, L. Zhang, W. Zhang, L. Li, T. Kawakami, K. Sugawara, T. Sato, G. Zhang, P. Gao, Y. Muhammad, X. Wen, B. Tao, F. Guo and H. Chang, *Adv. Funct. Mater.*, 2021, **31**, 2008116.
- 83 T. Dietl and H. Ohno, *Rev. Mod. Phys.*, 2014, **86**, 187–251.
- 84 X. L. Fan, Y. R. An and W. J. Guo, *Nanoscale Res. Lett.*, 2016, **11**, 154.
- 85 F. Zhang, B. Zheng, A. Sebastian, D. H. Olson, M. Liu, K. Fujisawa, Y. T. H. Pham, V. O. Jimenez, V. Kalappattil, L. Miao, T. Zhang, R. Pendurthi, Y. Lei, A. L. Elias, Y. Wang, N. Alem, P. E. Hopkins, S. Das, V. H. Crespi, M.-H. Phan and M. Terrones, *Adv. Sci.*, 2020, **7**, 2001174.
- 86 S. J. Yun, D. L. Duong, D. M. Ha, K. Singh, T. L. Phan, W. Choi, Y.-M. Kim and Y. H. Lee, *Adv. Sci.*, 2020, **7**, 1903076.
- 87 D. Shen, B. Zhao, Z. Zhang, H. Zhang, X. Yang, Z. Huang, B. Li, R. Song, Y. Jin, R. Wu, B. Li, J. Li and X. Duan, *ACS Nano*, 2022, **16**, 10623–10631.
- 88 K. Chen, X. Wan, W. Xie, J. Wen, Z. Kang, X. Zeng, H. Chen and J. Xu, *Adv. Mater.*, 2015, **27**, 6431–6437.
- 89 C. Chen, Y. Yang, X. Zhou, W. X. Xu, Q. N. Cui, J. B. Lu, H. M. Jing, D. Tian, C. X. Xu, T. Y. Zhai and H. Xu, *ACS Appl. Nano Mater.*, 2021, **4**, 5522–5530.
- 90 A. Y. Lu, H. Zhu, J. Xiao, C. P. Chuu, Y. Han, M. H. Chiu, C. C. Cheng, C. W. Yang, K. H. Wei, Y. Yang, Y. Wang, D. Sokaras, D. Nordlund, P. Yang, D. A. Muller, M. Y. Chou, X. Zhang and L. J. Li, *Nat. Nanotechnol.*, 2017, **12**, 744–749.
- 91 J. Zhu, W. Li, R. Huang, L. Ma, H. Sun, J. H. Choi, L. Zhang, Y. Cui and G. Zou, *J. Am. Chem. Soc.*, 2020, **142**, 16276–16284.
- 92 X. Bai, S. Li, S. Das, L. Du, Y. Dai, L. Yao, R. Raju, M. Du, H. Lipsanen and Z. Sun, *Nanoscale*, 2021, **13**, 4537–4542.
- 93 V. T. Vu, T. T. H. Vu, T. L. Phan, W. T. Kang, Y. R. Kim, M. D. Tran, H. T. T. Nguyen, Y. H. Lee and W. J. Yu, *ACS Nano*, 2021, **15**, 13031–13040.
- 94 C. Li, J. Zhu, W. Du, Y. Huang, H. Xu, Z. Zhai and G. Zou, *Nanoscale Res. Lett.*, 2021, **16**, 123.
- 95 Y. J. Lai, J. y Tan, Z. y Cai, R. Zhang, C. Teng, S. Zhao, J. Lin and B. Liu, *APL Mater.*, 2021, **9**, 051123.
- 96 H. Yu, M. Liao, W. Zhao, G. Liu, X. J. Zhou, Z. Wei, X. Xu, K. Liu, Z. Hu, K. Deng, S. Zhou, J.-A. Shi, L. Gu, C. Shen, T. Zhang, L. Du, L. Xie, J. Zhu, W. Chen, R. Yang, D. Shi and G. Zhang, *ACS Nano*, 2017, **11**, 12001–12007.